



ZERO BRINE

Software Tool for the Simulation of selected Brine
Treatment Technologies

Technology Libraries and integrated Platform



Deliverable 5.2	Name of deliverable
Related Work Package	WP5 - Software Tools for the simulation of selected brine treatment technologies (technology libraries and integrated platform)
Deliverable lead	DLR
Author(s)	DLR: Massimo Moser, Marina Micari, Benjamin Fuchs CTM: Joan Farnós
Contact	massimo.moser@dlr.de
Reviewer	Prof. Andrea Cipollina (Unipa)
Grant Agreement Number	730390
Instrument	Horizon 2020 Framework Programme
Start date	1.6.2017
Duration	18 months
Type of Delivery (R, DEM, DEC, Other)¹	R / Other
Dissemination Level (PU, CO, CI)²	PU
Date last update	30. Nov 2018
Website	www.zerobrine.eu
Name of researcher(s) with roles	

Revision no	Date	Description	Author(s)
0.1	19. Sep 2018	First draft	Massimo Moser
0.2	12. Oct 2018	Technology Models CTM	Joan Farnós
0.3	22. Oct 2018	Technology Models DLR	Marina Micari
0.4	22. Oct 2018	RCE Platform Description and Setup	Ben Fuchs
1.0	22. Oct 2018	First review, first consolidated version	Massimo Moser
1.1	31. Oct 2018	Various Updates	DLR/CTM
2.0	25. Nov 2018	Review UNIPA	Andrea Cipollina
2.1	28. Nov 2018	Minor refurbishments	M. Micari, J. Farnos
2.2	30. Nov 2018	Consolidated version	Massimo Moser

¹ R=Document, report; DEM=Demonstrator, pilot, prototype; DEC=website, patent fillings, videos, etc.; OTHER=other

² PU=Public, CO=Confidential, only for members of the consortium (including the Commission Services), CI=Classified

Table of Contents

1.	Introduction and Objectives.....	4
2.	Data Providers.....	4
3.	Data Management and Time Schedule.....	5
3.1.	Technical Data	5
3.2.	Time Schedule	7
4.	Multi-Effect Distillation Model.....	7
4.1.	Forward Feed Model	10
4.2.	Thermal Vapour Compressor	13
4.3.	MED Model Validation	13
4.4.	MED Nomenclature.....	15
5.	Reverse Osmosis Model.....	16
5.1.	RO Membrane	17
5.2.	RO Element.....	19
5.3.	RO Plant	20
5.4.	RO Model Validation.....	22
5.5.	RO Nomenclature	22
6.	Nanofiltration Model.....	23
6.1.	DSMP-DE Membrane Model.....	24
6.2.	NF Element and Plant Model	27
6.3.	NF Model Validation	28
6.4.	NF Nomenclature	28
7.	Crystallizer Model.....	30
7.1.	Crystallizer Nomenclature	33
8.	Membrane Distillation Model	34
8.1.	DCMD Element Model – Heat and Mass Transfer	35
8.1.1.	Heat Transfer	36
8.1.2.	Mass Transfer	38
8.2.	DCMD Unit Model – Mass and Energy Balances	40
8.3.	DCMD Plant Model	41
8.4.	MD Nomenclature	43
9.	Ion Exchange Resins Model.....	44
9.1.	Model for IEX Resins for Water Softening	45
9.2.	IEX Nomenclature	50

10.	Eutectic Freeze Crystallization Model	51
10.1.	Data driven numerical Model	51
10.2.	Thermodynamic EFC Model	51
10.3.	Experimental Validation	57
10.3.1.	Objective	57
10.3.2.	Experimental Campaign	57
11.	Process Models and Simulation Tools for Electrodialysis	60
11.1.	Nernst-Planck based Models	62
11.2.	Semi-empirical Models	63
11.3.	Simplified Models for the Simulation and Design of ED Systems.....	64
11.4.	Proposed Electro-Dialysis numerical Model ($V_{\text{tank}}=cte$)	65
11.5.	Renewable Energy Integration	70
11.6.	Deliverables	71
12.	RCE Integration	71
12.1.	RCE	71
12.2.	RCE Server	72
12.3.	The RCE Client	73
12.4.	Tool Integration.....	73
12.5.	Technical Aspects of RCE.....	74
12.6.	Progress on the RCE Integration of Tools	74
13.	Conclusion	Error! Bookmark not defined.
14.	Bibliography	74

1. Introduction and Objectives

The ZERO BRINE project aims to facilitate the implementation of the Circular Economy package and the SPIRE roadmap in various process industries by developing necessary concepts, technological solutions and business models to redesign the value and supply chains of minerals and water while dealing with present organic compounds in a way that allows their subsequent recovery.

Minerals and water will be recovered from saline impaired effluents (brines) generated by the process industry while eliminating wastewater discharges and minimizing the environmental impacts of industrial operations through brines (ZERO BRINE). ZERO BRINE brings together and integrates several existing and innovative technologies to recover products of high quality and sufficient purity to represent good market value.

The objective of this task is to develop a software tool that will be used for the simulation of different brine treatment trains selected throughout the project implementation in order to treat different complex brine streams. To do so, technology libraries will be developed for each of the technologies that will be used. These libraries will build upon previous experience of partners, using various programming environments, namely Python and Matlab. In a second step, a common simulation platform will be set up in order to simulate the complete treatment chains proposed in WP2-WP4. The implemented tool will be then used in the case studies of WP7. Matlab (matrix laboratory) is a powerful numerical computing environment, which has been commercially developed by Mathworks over the last 34 years. Matlab is mainly intended for numerical computing, nevertheless it offers a series of additional toolboxes for symbolic computing as well as graphical multi-domain simulation). This software will be used by CTM to carry out the simulation of the heat recovery systems, the eutectic freeze crystallization (TU DELFT-EFC) technologies as well as the electrodialysis (ED). Python is a high-level programming language for general-purpose programming. Based on previous works carried out at the DLR, Python is used to model several water treatment technologies such as MED (plane and with thermal vapour compression (TVC)), reverse osmosis (RO), nanofiltration (NF) and the CrIEM crystallizer. DLR is the responsible for the implementation of this Task, in close collaboration with the technology suppliers of the project. The software tool developed in this task will also be used to assess the replicability of the treatment trains in other process industries during WP7 and WP8, where at least two industries will be selected to replicate the results in the Netherlands.

2. Data Providers

Data providers are responsible for acquisition of the data, processing and visualization of the data and delivery all the data to the data manager. Most of the data from WP5 regarding EFC will be obtained thorough bench-scale and pilot scale experimentation. In the following table, the data providers for each process or technology are defined.

Table 1: Data provided from each partner in WP5, task 5.3

Partner	Data provided
---------	---------------

DLR	Leading partner
CTM	CTM is the responsible of WP5 EFC modelling, thus CTM will be the data manager. In addition, CTM is the responsible to perform bench scale experiments and produce experimental data from bench scale experimentation related to membrane regeneration process, NF/RO technology, EFC and EDBP. In addition, CTM will analyze samples from pilot plant and will process all the generated data with the support of the rest of the partners. CTM also will evaluate heat waste recovery strategies creating theoretical data related to this process.
UNIPA	Unipa will deliver support for the modeling activities. In particular, support will be given to DLR with regard to the validation of the MED model. In addition, Unipa will deliver basic information about the modeling of the crystallizer.
FACSA	FACSA will provide techno-economic information which will be useful for the upcoming activities of WP7 (feasibility studies)
SEALEAU	DLR will provide some support to Sealeau for the MED design
LENNTECH	Lenntech will help DLR providing validation data for the characterization of the NF model
TYPSA	TYPSA will provide techno-economic information which will be useful for the upcoming activities of WP7 (feasibility studies)
TUdelft	TUdelft will provide data by eutectic freeze crystallization, as technology provider of EFC.
NTUA	NTUA provided information regarding the MED pilot plant

3. Data Management and Time Schedule

3.1. Technical Data

The Database from WP5 will contain mainly technical information, experimental and observational Data.

Experimental data includes all the data generated during experimentation at bench scale and at pilot scale. This data will be collected by the person responsible for the experiments and send to the person coordinating the task and finally to the WP5 leader. The following table shows the data produced from experimentation.

Table 2: Experimental data obtained for each process/technology

Technology/process	Data produced
--------------------	---------------

Technology/process	Data produced
NF/RO	<p>Operation parameters: applied pressure; recirculation flow, permeate recovery, permeate flux. Literature data for: antiscalant dosage, cleaning operations, etc.</p> <p>Quality parameters: permeate (produced water) and concentrate composition. For permeate conductivity will be the most critical parameter.</p> <p>Cost parameters: energy requirements with and without waste heat recovery, chemicals, investments costs, membranes cost.</p>
EFC	<p>Operation conditions: temperature; feed flow,</p> <p>Quality parameters: Na₂SO₄ purity, water produced quality.</p> <p>Cost parameters: energy requirements with and without waste heat recovery, investments costs.</p>
MED	<p>Operation conditions: temperature; feed flow, etc.</p> <p>Quality parameters: concentrate brine concentration, water produced quality.</p> <p>Cost parameters: energy requirements with and without waste heat recovery, investments costs.</p>
EDBP	<p>time; voltage, current, and current density (calculated); flow rate of feed, diluate, acid and base concentrate</p> <p>Quality parameters: NaON and H₂SO₄ concentration, water produced quality.</p> <p>Cost parameters: energy requirements, investments costs.</p>
CrIEM/Crystallizer	<p>Operation condition: feed flow; alkaline solution concentration; feed concentration of Mg⁺⁺ and Ca⁺⁺</p> <p>Quality parameters: effluent composition, fractionated crystallisation efficiency, purity of crystals.</p>

3.2. Time Schedule

Task	Responsible	Deadline
Definition of the study methodology	CTM	October 2017
Final MED Model	DLR	October 2017
Final RO Model	DLR	February 2018
Waste heat sources characterization	CTM	March 2018
Gather information regarding the EU silica industry	CTM	March 2018
Final Crystallizer Model	DLR	March 2018
Final NF Model	DLR	July 2018
RCE server installed	DLR	July 2018
Final MD Model	DLR	September 2018
RCE model integration test	DLR	October 2018
Final IEX Model	DLR	October 2018
RCE server fully functional and model test integrations carried out for DLR and CTM	DLR/CTM	November 2018
Definition of the energy monitoring system for the EFC/Evaporator technologies operation at the pilot scale.	CTM	November 2018

4. Multi-Effect Distillation Model

The technical/design model of the Multi-Effect distillation process is mainly based on mass and energy balances at steady-state conditions and on the evaluation of thermo-physical properties of water, in the liquid or in the vapor state, and of the NaCl-water solution. These properties are estimated via correlations reported in literature. The main input variables are: feed salinity, temperature and flow rate, steam temperature, motive steam pressure (in presence of the TVC), required brine salinity, temperature of the last effect and number of effects. All the geometrical features, such as the size of the tubes in the tube bundles or of the connecting lines, are given as

parameters. Conversely, the key output variables of the design model are the heat exchanger areas, the preheater areas and the end-condenser area, the steam flow rate and the motive steam flow rate in the case of the MED-TVC.

The model takes advantage from a purposely developed resolution algorithm which includes minimization steps (via iterative procedures) allowing design requirements to be fulfilled. The model is able to run for different feed arrangements (FF-MED and PC-MED) and different design methods, which refer to different design requirements, i.e. one provides equal A_{HX} and equal A_{preh} , while the other provides equal temperature differences (ΔT_{eff}) for each effect. In general, for easiness of comparison with other technical models, the design method with equal areas of the heat exchangers and the preheaters was selected.

Table 3: Main inputs and outputs of the technical model for the MED process

Model	Inputs	Outputs
Technical model	Number of effects (N [-])	Distillate flow rate (M_{dist} [kg/s])
	Feed flow rate (M_{feed} [kg/s])	Brine flow rate (M_{brine} [kg/s])
	Feed salinity (X_{feed} [ppm])	Heat exchanger areas (A_{HX} [m ²])
	Intake feed temperature (T_{feed} [°C])	Preheater areas (A_{preh} [m ²])
	Brine salinity (X_{brine} [ppm])	End-condenser area (A_{cond} [m ²])
	Steam temperature (T_s [°C])	Cooling-water flow rate (M_{cw} [kg/s])
	Motive steam pressure (P_m [bar])	Steam flow rate (M_s [kg/s]) and motive steam flow rate for MED-TVC (M_m [kg/s])
	Temperature in the last effect (T_N [°C])	Specific area (sA [m ² /(kg/s)]) and specific thermal consumption (sQ [kJ/kg])

The structure of the resolution algorithm is reported in **Figure 1**. As shown in the figure, the technical model presents three minimization loops, since it is required that (i) the areas of the heat exchangers (A_{HX}) and (ii) the areas of the preheaters (A_{preh}) have to be equal and (iii) a given distillate flow rate (M_{dist}) has to be produced which corresponds to a given brine salinity.

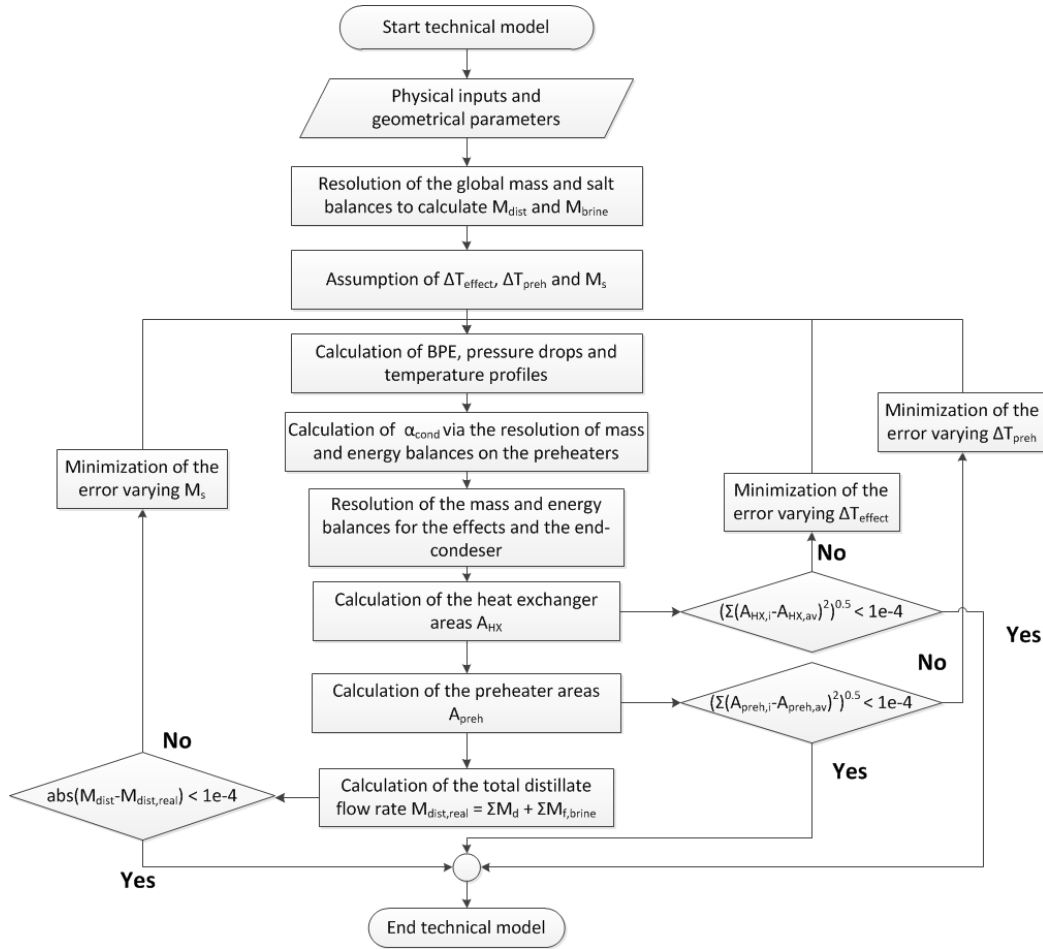


Figure 1: Resolution algorithm for the MED model

The main output variables are the specific area (sA), the specific thermal consumption (sQ) and the GOR, which are defined as follows.

$$(4.1) \quad sA = \frac{\sum_N A_{HX} + \sum_{N-1} A_{preh} + A_{cond}}{M_{dist}}$$

$$(4.2) \quad sQ = \frac{M_s \lambda(T_s)}{M_{dist}}$$

$$(4.3) \quad GOR = \frac{M_s}{M_{dist}}$$

Where $\lambda(T_s)$ is the latent heat of water at a temperature equal to T_s .

In this report, a more detailed description of the FF-MED plant is reported because of the high concentrations and the high Top Brine Temperatures (El-Dessouky et al. 1998), which are common to most of the cases investigated by the Zero Brine project.

4.1. Forward Feed Model

The schematic representation of the MED plant described in the present FF-MED model is reported in **Figure 2**. It shows the first effect, a generic intermediate effect and the last effect with the end condenser. In fact, three slightly different systems of mass and energy balance equations have been used to model these three classes of effects.

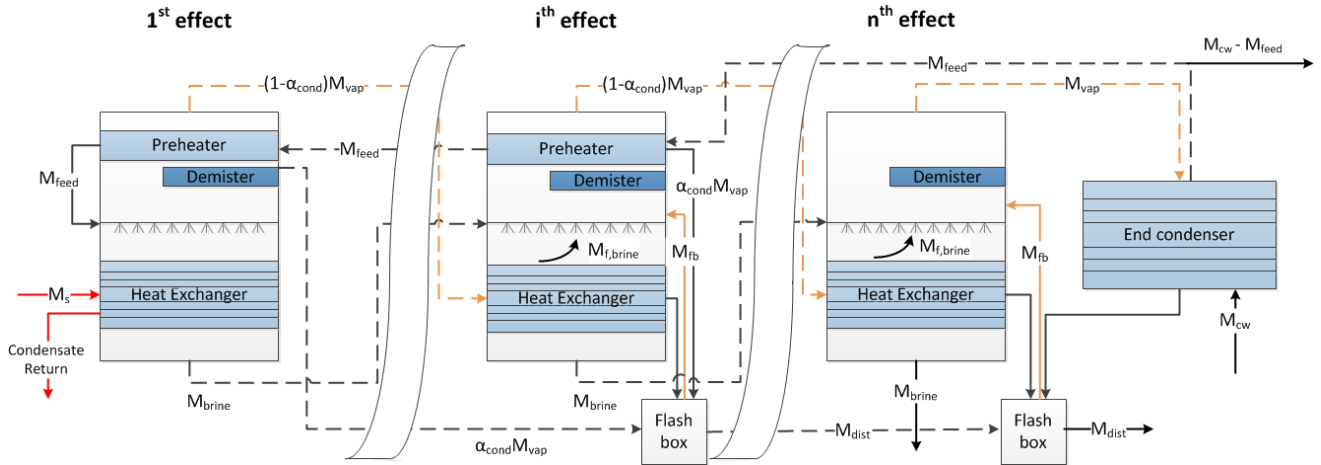


Figure 2: Schematic representation of the MED plant

All the equations relevant to the model of the FF-MED are reported in Table 4, where λ is the latent heat of water, h_{vap} is the enthalpy of the steam, h_{liq} is the enthalpy of the liquid water, h_{sw} is the enthalpy of the NaCl salt-water solution and $c_{p,sw}$ is the NaCl salt-water solution specific heat. The water properties are function of temperature, while the NaCl-water solution properties are functions of temperature and composition. Basically, each run starts from the calculation of global mass and salinity balances, to estimate the brine flow rate (M_{brine}), the distillate flow rate (M_{dist}) and the brine salinity (X_{brine}), having assumed that the distillate is pure water. Then, all the variables, such as mass flow rate, temperature and pressure, related to each single effect are estimated.

Table 4: Main mass and energy balance equations of the forward-feed MED model

(4.4)	$M_{feed} = M_{dist} + M_{brine}$	Global mass balance
(4.5)	$M_{feed} X_{feed} = M_{brine} X_{brine}$	Global salt balance
(4.6)	$T_{vsat} = T - BPE(T, X_{brine})$	Temperature drop for the BPE
(4.7)	$T'_{vsat} = T_{vsat} - \Delta T_{demister}$	Temperature drop in the demister
(4.8)	$T'_c = T'_{vsat} - \Delta T_{lines}$	Temperature drop in the connecting lines
(4.9)	$T_c = T'_c - \Delta T_{grav} - \Delta T_{acc}$	Temperature drop in the evaporator
(4.10)	$M_s \lambda(T_s) + M_{feed} h_{sw}(T_{preh}[1], X_{feed})$ $= M_b[1] h_{sw}(T[1], X_b[1])$ $+ (1 - \alpha_{cond}[1]) M_{vap}[1] h_{vap}(T'_{vsat}[1])$ $+ \alpha_{cond}[1] M_{vap}[1] h_{liq}(T'_{vsat}[1])$	Energy balance on the first effect
(4.11)	$M_b[i - 1] = M_d[i] + M_{fbrine}[i] + M_b[i]$	Mass balance on a generic effect
(4.12)	$M_{feed} X_{feed} = M_b[i] X_b[i]$	Salt balance on a generic effect
(4.13)	$M_{vap}[i] = M_d[i] + M_{fbrine}[i] + M_{fb}[i]$	Mass balance on the vapor phase
(4.14)	$M_c[i - 1] + \alpha_{cond}[i] M_{vap}[i]$ $+ (1 - \alpha_{cond}[i - 1]) M_{vap}[i - 1] = M_{fb}[i] + M_c[i]$	Mass balance on the generic flash-box
(4.15)	$M_c[i - 1] h_{liq}(T'_{vsat}[i - 1])$ $+ \alpha_{cond}[i] M_{vap}[i] h_{liq}(T'_{vsat}[i]) +$ $(1 - \alpha_{cond}[i - 1]) M_{vap}[i - 1] h_{liq}(T_c[i - 1])$ $= M_{fb}[i] h_{vap}(T'_{vsat}[i]) + M_c[i] h_{liq}(T'_{vsat}[i])$	Energy balance on the generic flash-box
(4.16)	$M_{fbrine}[i] \lambda(T_{brine, f}[i])$ $= M_{brine}[i - 1] c_{p,sw}(T_{mean}, X_b[i - 1])$ $(T[i - 1] - T_{brine, f}[i])$	Energy balance on the brine entering as the feed ($T_{brine, f}$ calculated via the Non Equilibrium Allowance (El-Dessouky et al. 1998))
(4.17)	$M_{feed} c_{p,sw}(T_{mean}, X_f) (T_{preh}[i] - T_{preh}[i + 1])$ $= \alpha_{cond}[i] M_{vap}[i] \lambda(T'_{vsat}[i])$	Energy balance on a generic preheater
(4.18)	$(1 - \alpha_{cond}[i - 1]) M_{vap}[i - 1] \lambda(T_c[i - 1])$ $+ M_{fbrine}[i] (h_{sw}(T[i - 1], X_b[i - 1]) - h_{vap}(T'_{vsat}[i]))$ $+ M_b[i] (h_{sw}(T[i - 1], X_b[i - 1]) - h_{sw}(T[i], X_b[i]))$ $= M_d[i] (h_{vap}(T'_{vsat}[i]) - h_{sw}(T[i - 1], X_b[i - 1]))$	Energy balance on a generic heat exchanger
(4.19)	$(1 - \alpha_{cond}[N - 1]) M_{vap}[N - 1] \lambda(T_c[N - 1])$ $+ M_{fb}[N] h_{vap}(T'_{vsat}[N])$ $+ M_b[N - 1] h_{sw}(T[N - 1], X_b[N - 1])$ $= M_b[N] h_{sw}(T[N], X_b[N])$ $+ M_{vap}[N] h_{vap}(T'_{vsat}[N])$	Energy balance on the last effect
(4.20)	$M_{cw} c_{p,sw}(T_{cw}, X_{feed}) (T_{cw, out} - T_{cw, in}) = M_{vap}[N] \lambda(T'_c[N])$	Energy balance on the end condenser

Regarding the temperature profiles, six main quantities have to be calculated: temperature of the brine generated in the effect (T), temperature reached by the feed in the preheater of the effect (T_{preh}), temperature of the saturated vapor generated in the effect (T_{vsat}), temperature of the vapor after crossing the demister (T'_{vsat}), temperature of the vapor after crossing the connecting lines (T'_c)

and condensation temperature of the vapor in the following effect (T_c). These are interdependent according to the equations (4.6)-(4.9), through the boiling point elevation (BPE) and the pressure drops, which lead to temperature drops ($\Delta T_{\text{demister}}$, ΔT_{lines} , ΔT_{grav} , ΔT_{acc}), in the case of saturated vapor. The boiling point elevation is estimated through the Pitzer model, which is valid in a wider range of salinity compared to the other correlations in literature (Pitzer and Mayorga 1973, M. Bialik et al. 2008). The pressure drops are estimated according to some correlations present in literature (ESDU 1993, Shen 2015). Concerning the modelling of the effects, the first effect is the only one which receives heat from an external source (M_s at temperature equal to T_s) and in which the feed (M_{feed} at a concentration equal to X_{feed}) enters after having crossed all the preheaters. The feed is sprayed on a tube bundle, while M_s flows inside the tubes. In this effect, the vapor generated (M_{vap}) is given only by the partial evaporation of the feed (M_d). This crosses the demister and the first preheater, where it partially condenses. The remaining part is sent to the following effect, as the heating steam. The brine generated in the first effect (M_b at a concentration equal to X_b) is sent to the following effect as the feed, sprayed on the external surface of the tube bundle. The intermediate effects' modelling includes the two energy balances on the preheater and on the heat exchanger to know the condensed fraction on the preheater tube surface (α_{cond}) and M_d , respectively (equations (4.17)-(4.18)). Moreover, other two vapor contributions have to be considered: the vapor generated by the inlet brine flash (M_{brine} from equation (4.16)) and the vapor coming from the flashing box M_{fb} , which is generated by the flash of the condensed distillate collected in the flashing box (M_{fb} and M_c , the condensate exiting from the flash box, are derived from equation (4.14), (4.15)). Finally, the last effect differs from the others because it does not have any preheater and the entire vapor generated in the last effect is sent to the end condenser, where it condenses completely. This leads to a slight different expression of the energy balances on the effect (Equation (4.19)) and on the last flashing box, since the total M_{vap} generated in the last effect is condensed in the end condenser and then collected in the flash box. The brine generated in the last effect ($M_b [N]$) constitutes the final brine produced by the plant, while the condensate exiting from the last flash box ($M_c [N]$) constitutes the final distillate. These have to satisfy the global balance in Equations (4.4)-(4.5). Regarding the end condenser, usually, the feed itself is used to condensate the vapor. The necessary total cooling water flow rate (M_{cw}) is calculated through the heat balance reported in Equation (4.20) and the surplus ($M_{\text{cw}} - M_{\text{feed}}$) is cooled down and can be reused.

As already mentioned, the required steam flow rate M_s is calculated through the minimization loop and this figure is necessary to calculate the thermal energy requirement of the whole system which is defined as the product of the steam flow rate times the latent heat at T_s . For what concerns the electric energy requirement, this takes into account the energy requirement of the pumps and it is assumed equal to $1.5 \text{ kWh}_{\text{el}}/\text{m}^3$ (Sommariva 2010).

Finally, the areas of the heat exchangers, of the preheaters and of the end condenser are calculated according to Equations (4.21)-(4.24), where $DTML_{\text{preh}}$ and $DTML_{\text{cond}}$ are the temperature logarithmic mean in the preheater and in the condenser and U_{cond} and U_{evap} are the heat transfer coefficients for the condenser and the evaporator respectively, derived from correlations by El-Dessouky et al. (El-Dessouky et al. 1998)

Table 5: Equations to calculate the heat exchangers, preheaters and end condenser areas of the MED plant

$$(4.21) \quad A_{hx} [0] = \frac{M_{feed} c_{p_{sw}}(T_{mean}, X_f)(T[1] - T_{preh}[1]) + M_d[1] \lambda(T_{vsat}[1])}{U_{evap}(T[1])(T_{steam} - T[1])}$$

$$(4.22) \quad A_{hx} [i] = \frac{(1 - \alpha_{cond}[i - 1])M_{vap}[i - 1] \lambda(T_c[i - 1])}{U_{evap}(T[i])(T_c[i - 1] - T[i])}$$

$$(4.23) \quad A_{preh} [i] = \frac{\alpha_{cond}[i] M_{vap}[i] \lambda(T'_{vsat}[i])}{U_{cond}(T'_{vsat}[i]) DTML_{preh}}$$

$$(4.24) \quad A_{cond} = \frac{M_{cw} c_{p_{sw}}(\overline{T_{cw}}, X_{feed})(T_{cw,out} - T_{cw,in})}{U_{cond}(T'_c[N]) DTML_{cond}}$$

4.2. Thermal Vapour Compressor

In the case of a MED-TVC system, a certain amount of vapor generated in the last effect is not condensed in the end condenser but it is recycled to the first effect as part of the heating steam. More in detail, this is possible using a compression device, such as a thermo-compressor, in which a fraction of the vapor coming from the last effect or from an intermediate (i.e. entrained vapor) is mixed with the vapor coming from an external source (i.e. motive steam). In this work, the entrained vapor is always taken from the last effect. The discharged vapor is rejected as super-heated vapor at a pressure equal to the saturation pressure at $T=T_s$. In order to model the TVC, some correlations reported in literature were employed (El-Dessouki and Ettouney 2002, Hassan and Darwish 2014). Given the pressure of the motive steam P_m , the saturation pressure at T_s (P_s) and the pressure of the entrained vapor (P_{ev} , i.e. the saturation pressure at T_n), it is possible to calculate the compression ratio ($C_R = P_s / P_{ev}$) and the expansion ratio ($ER = P_m / P_{ev}$). Thus, the correlations allow calculating the entrainment ratio ($Ra = M_m / M_{ev}$) and, consequently, the amount of steam, which has to be supplied externally (M_m).

4.3. MED Model Validation

The described model was validated through the comparison with another model, which is present in literature (Ortega-Delgado et al. 2017). The two models are similar in their structure, both of them are employed as design models in which the areas of the heat exchangers and of the preheaters are imposed equal. Moreover, the thermo-physical properties of the salt solutions are estimated as functions of temperature and composition. The main differences consist in the estimation of the Boiling Point Elevation (BPE), which is estimated through the Pitzer model in the present model, in order to be able to cover a wider range of feed and brine salinity. Conversely, in the reference model the correlation reported by Sharqawy et al. for seawater was used (Sharqawy et al. 2010). This last correlation and the Pitzer model shows a good agreement at low concentrations, although the BPE calculated via the Pitzer model is higher, while at concentrations higher than 120 g/kg the correlation by Sharqawy is not valid. Also the programming method is different, since the present model is

implemented in Python and a suitable resolution algorithm had to be developed, while the model by Ortega-Delgado et al. is implemented in Engineering Equation Solver (EES) and a simultaneous solver system is employed, which uses the Newton-Raphson method. For validation purposes, the models were tested within the typical desalination range of concentration (35,000-65,000 ppm) and some simulation analyses, varying the number of effects and the distillate flow rate, were carried out, both for the Forward Feed and for the Parallel Cross arrangement. For sake of brevity, only the results of the analysis performed varying N for the forward-feed MED-TVC are reported. The inputs used for this analysis are reported in Table 6.

Table 6: Inputs for the reported validation analysis (variation of N_{effects})

X_{feed} [ppm]	35,000
X_{brine} [ppm]	65,000
N [-]	variable (4-15)
T_{steam} [°C]	70
$P_{\text{motive steam}}$ [bar]	3.5
T_n [°C]	38
M_{feed} [kg/s]	5

Figure 3 shows a very good agreement between the two models. The slight difference which is reported for higher number of effects is due to the fact that the BPE estimated in the Python model through the Pitzer equations is always higher than the one estimated in the EES model. This determines a slight difference in the areas especially at higher number of effects, where the operating ΔT of each effect is lower. As the number of effects increases, the specific area increases because of the depletion of the driving force which is available for the single effect. At the same time, the higher the number of effects, the higher the thermal efficiency of the system. Therefore, the required motive steam decreases and the GOR increases with N.

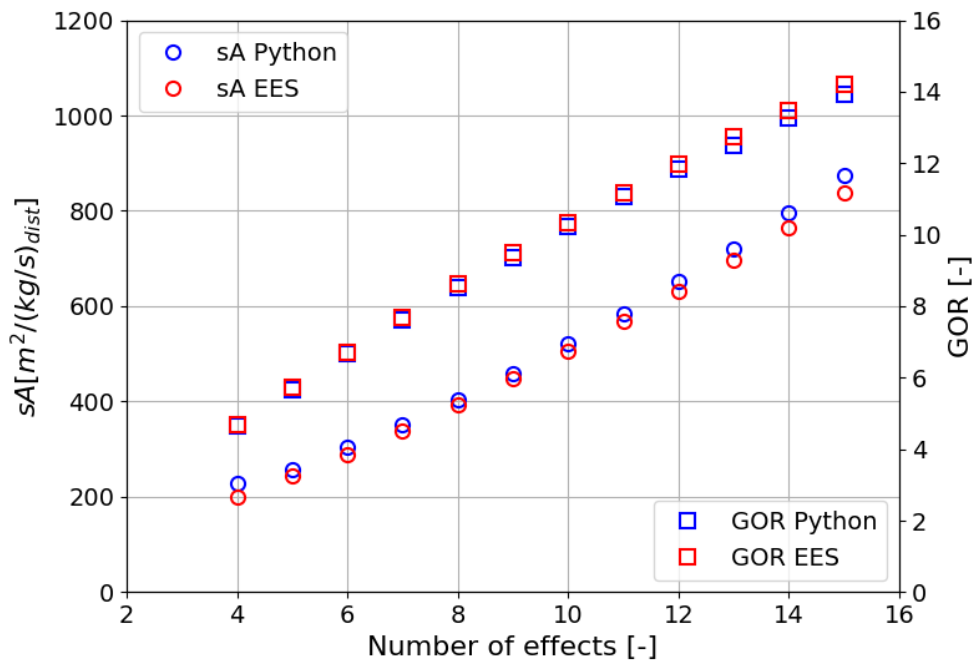


Figure 3: Comparison of the specific area [$\text{m}^2/(\text{kg/s})_{\text{dist.}}$] and the GOR [-] as functions of the number of effects for the present model (Python model) and for the reference model (EES model) for the case of a MED-TVC system with a forward-feed arrangement.

4.4. MED Nomenclature

N	number of effects [-]
M	mass flow rate [kg/s]
T	temperature [°C]
X	salinity [ppm]
P	pressure [bar]
A	heat exchanger area [m^2]
sA	specific area [$\text{m}^2/(\text{kg/s})$]
sQ	specific thermal consumption [kJ/kg]
h	specific enthalpy [kJ/kg]
C_p	specific heat [kJ/(kg °C)]
U	overall heat transfer coefficient [kW/(m^2 °C)]
C_R	compression ratio [-]
ER	expansion ratio [-]
Ra	entrainment ratio [-]

Greek letters

λ	latent heat [kJ/kg]
ΔT	temperature difference [°C]
α_{cond}	fraction of vapor condensed in the preheater

Subscripts

feed	feed entering into the first effect
dist	outlet distillate

brine	outlet brine
HX	heat exchanger
preh	preheater
cond	end-condenser
s	total steam
m	motive steam
vap	total vapor generated in the generic effect
d	vapor generated via evaporation
f,brine	vapor generated via the brine flash
fb	vapor generated in the flash box
b	brine solution generated in the generic effect
c	condensed pure water collected in the flash box
cw	cooling water
sw	salt water solution
liq	pure water in the liquid state
vap	pure water in the vapor state
n	last effect index
ev	entrained vapor
_real	fixed distillate flow rate to be produced

Acronyms

MED	Multi-Effect Distillation
TVC	Thermo-vapor compressor
GOR	Gain Output Ratio
FF	Forward Feed
BPE	Boiling Point Elevation [°C]
DTML	Temperature logarithmic mean

5. Reverse Osmosis Model

Reverse Osmosis is one of the most common desalination processes, which is based on a membrane separation under an applied pressure. RO is widely used for seawater desalination to obtain potable water. However, it is effective in treating water at any salinity, from brackish water up to high salinity waters. The technology is commonly present at the industrial scale and several efforts were made to produce highly performing membranes, with very high salt rejection (approx. 99%) and high water flux (Wilf 2007). The most common configuration presents a spiral-wound geometry and the RO plant arrangement consists in a certain number of pressure vessels in parallel, each of those containing a certain number of RO elements in series (typically between 4 and 8) (Vince et al. 2008). Depending on the operating conditions, e.g. the feed concentration, and on the main objective of the separation, e.g. high purity water as permeate, it is possible to select different possible configurations, such as single stage, double stage with permeate staging, double or multiple stage with concentrate staging (Malek et al. 1996). Two of the main issues of the RO process regard the concentration polarization and the membrane fouling, which are connected and contribute both in

water flux depletion and eventually higher energy consumption. Several methods have been used to reduce these effects, for example increasing the flow rate or promoting turbulence (Jamal et al. 2004). For what concerns the literature about the RO modelling, some analytical models have been developed to estimate the transport phenomena across the RO membrane (Lonsdale et al. 1965, Kimura and Sourirajan 1967). Moreover, commercial software developed by DOW is available and allows the simulation of several membrane elements and configurations. Some studies are also devoted to the comparison between single and multi-stage operations (Malek et al. 1996) or to the optimization of the process configuration (Vince et al. 2008).

The model set up for the simulation of the RO process within the Zero Brine project provides the possibility to simulate a single stage or a multi-stage system and it is an optimization model which finds the suitable feed pressure in correspondence to a certain recovery. The model starts from the evaluation of the membrane properties and the calculation of water and salt flux under a certain pressure. Thus, the whole element is taken into account and discretized along the length in a certain number of sub-elements. In each of those, trans-membrane fluxes are calculated and mass balances are applied. Finally, the elements are interconnected to simulate the pressure vessel and the whole plant. The structure of the RO plant, as it is described by the implemented model is reported in Figure 4.

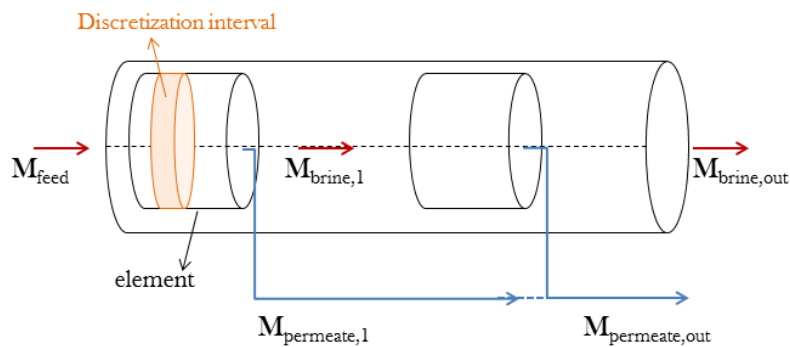


Figure 4: Structure of a single stage RO plant

5.1. RO Membrane

The model commonly used to simulate the RO membrane performances is a two-parameter solution diffusion model which provides that both water and solute diffuse through the membrane and their transport is regulated by two parameters: pure water permeability in the membrane (A_{membr}) and solute permeability in the membrane (B_{membr}). Therefore, the water flux (F_w) and the solute flux (F_s) through the membrane are defined as follows:

$$(5.1) \quad F_w = A_{membr} (\Delta P - \Delta \Pi)$$

$$(5.2) \quad F_s = B_{membr} (X_{f,w} - X_p) 10^{-6}$$

where ΔP is the transmembrane pressure difference [bar], $\Delta \Pi$ is the transmembrane osmotic pressure difference [bar], $X_{f,w}$ is the feed concentration at the solution-membrane interface [ppm]

and X_p is the permeate concentration, which is usually negligible in this expression in comparison with $X_{f,w}$. The osmotic pressure difference is calculated according to the Van't Hoff relation:

$$(5.3) \quad \Delta\Pi = \frac{2 RT \rho}{M_{NaCl}} 10^{-5} (X_{f,w} - X_p) 10^{-6}$$

where R is the universal gas constant, T is the operating temperature [K], ρ is the solution density [kg/m^3] and M_{NaCl} is the molar mass of NaCl (0.0585 kg/mol). In the case of other components present in the solution, the osmotic pressure depends on the sum of the concentration differences between feed and permeate side divided by the relevant molar mass of the component.

The membrane properties are calculated starting from some data supplied by the membrane produced, as reported for two membranes taken as examples in Table 7.

Table 7: Nominal test conditions for two types of membranes (FILMTEC RO Membranes)

Membrane	Active area [m^2]	Pressure [bar]	Permeate flow rate [m^3/day]	Rejection [%]	Concentration [ppm]	Salt
SW30XLE-440	40.9	55.2	37.5	99.8	32,000	NaCl
BW30HRLE-440	40.9	10.3	47.9	99.3	2,000	NaCl

The estimation of the nominal membrane properties is performed calculating the osmotic pressure at the test condition and then applying the definition of water and solute flux to calculate $A_{\text{membr,nom}}$ and $B_{\text{membr,nom}}$ respectively.

$$(5.4) \quad \Delta\Pi_{\text{test}} = \frac{2 RT \rho}{M_{NaCl}} 10^{-5} X_{f,\text{test}} 10^{-6}$$

$$(5.5) \quad A_{\text{membr,nom}} = \frac{F_{w,\text{test}} 1000}{24 \times 3600 A (\Delta P_{\text{test}} - \Delta\Pi_{\text{test}})}$$

$$(5.6) \quad B_{\text{membr,nom}} = \frac{1 - R_{\text{salt}}}{R_{\text{salt}}} A_{\text{membr,nom}} (\Delta P_{\text{test}} - \Delta\Pi_{\text{test}})$$

where $X_{f,\text{test}}$ is the feed concentration in the test condition [ppm], $F_{w,\text{test}}$ is the flow in m^3/day , ΔP_{test} is the transmembrane pressure in the test condition, A is the active area [m^2] and R_{salt} is the membrane salt rejection.

The real values of the membrane properties, i.e. A_{membr} and B_{membr} are calculated by correcting the nominal values with the temperature correction factor (TCF) and the membrane ageing factors (MAF_w and MAF_s), which are calculated as follows:

$$(5.7) \quad TCF = \frac{1}{e^{C_{\text{membr}} \left(\frac{1}{T} - \frac{1}{298} \right)}}$$

$$(5.8) \quad MAF_w = (1 - \Delta\Phi_w)^{\text{age}_{\text{membr}}}$$

$$(5.9) \quad MAF_s = 1 + \Delta\Phi_{s,\text{coeff}} \times \text{age}_{\text{membr}}$$

where C_{membr} is a constant, characteristic of membrane barrier material (around 2,500-3,000 for polyamide membranes (Wilf 2007)), $\text{age}_{\text{membr}}$ is the average life time of the RO membranes (taken equal to 4 years) and $\Delta\Phi_w$ and $\Delta\Phi_s$ are measures of the relative water passage loss and of the relative solute passage increase with time (equal to 0.07 and 0.1 respectively) (Wilf 2007, Moser 2015). Overall, the temperature increase has a positive impact on the membrane performances because the permeability of water is higher and the required pressure decreases. Conversely, the membrane performances decline with time because of the formation of fouling layers and the loss of mechanical stability. For this reason, it is observable a reduction of the water flux and an increase of the salt flux. Finally, the concentration of the feed solution at the feed-membrane interface ($X_{f,w}$) is estimated taking into account the concentration polarization phenomenon, through the following correlation, as a function of the membrane element recovery:

$$(5.10) \quad CPF = k_p e^{\left(\frac{2 R_{el}}{2 - R_{el}} \right)}$$

where the membrane element recovery R_{el} is defined as the ratio between the produced permeate flow rate and the feed flow rate, while k_p is a constant depending on membrane element geometry. The higher R_{el} , the higher CPF because the concentration of the feed increases more sharply in the element.

5.2. RO Element

The RO element is discretized along its length in a certain number of sub-elements (equal to 50, which resulted to be an accurate discretization on the basis of a sensitivity analysis) and for each element the water and salt fluxes are calculated. Thus, the permeate flow rate and composition are estimated as:

$$(5.11) \quad M_{\text{perm}}[i] = (F_w[i] + F_s[i]) \frac{A_{\text{elem}}}{n_{\text{discr}}}$$

$$(5.12) \quad X_{\text{perm}}[i] = \frac{F_s[i]}{F_w[i]} 10^6$$

The fluxes are calculated at the transmembrane pressure and the transmembrane osmotic pressure of the accounted sub-element and the feed pressure is assumed to vary linearly in every element with a pressure drop of each element of 0.5 bar (*Filmtec Reverse Osmosis Membranes Technical Manual* n.d.). The concentrate flow rate and concentration are calculated via mass balances:

$$(5.13) \quad M_{\text{conc}}[i] = M_f[i] - M_{\text{perm}}[i]$$

$$(5.14) \quad X_{\text{conc}}[i] = \frac{X_f[i] M_f[i] - X_{\text{perm}}[i] M_{\text{perm}}[i]}{M_{\text{conc}}[i]}$$

The outlet concentrate flow rate produced in the i element constitutes the inlet feed flow rate of the $i+1$ element.

$$(5.15) \quad M_f[i + 1] = M_{\text{conc}}[i]$$

$$(5.16) \quad X_f[i + 1] = X_{\text{conc}}[i]$$

Finally, the overall distillate produced in the element is the sum of the permeate solutions produced in every sub-element and its composition is calculated via a mass balance:

$$(5.17) \quad M_{\text{perm,out elem}} = \sum_i M_{\text{perm}}[i]$$

$$(5.18) \quad X_{\text{perm,out elem}} = \frac{\sum_i M_{\text{perm}}[i] X_{\text{perm}}[i]}{\sum_i M_{\text{perm}}[i]}$$

Finally, the element recovery can be calculated as:

$$(5.19) \quad R_{\text{el}} = \frac{M_{\text{perm,out elem}}}{M_{\text{feed elem}}} \times 100$$

5.3. RO Plant

The single stage RO plant is given by a certain number of pressure vessels in parallel, each of those presenting RO elements in series. The simulation of the pressure vessel provides the interconnection of the elements, described in the previous section, by the definition of the inlet feed flow rate of every element as the concentrate flow rate produced by the previous element. The permeate flow rate produced by every pressure vessel ($M_{\text{perm,out}}$) is the sum of the permeate solutions produced in every element contained in the vessel. The main performance indicators of the RO plant consist in the overall recovery, the purity of the outlet permeate solution $X_{\text{perm,out}}$ and the electric power consumption P_{RO} [kW] which is dominated by the power demand of the high pressure pump, given by:

$$(5.20) \quad R_{\text{plant}} = \frac{M_{\text{perm,out}}}{M_{\text{feed}}} \times 100$$

$$(5.21) \quad X_{\text{perm,out}} = \frac{\sum_{\text{elem}} M_{\text{perm,out elem}} X_{\text{perm,out elem}}}{M_{\text{perm,out}}}$$

$$(5.22) \quad P_{\text{RO}} = \frac{P_{\text{feed}} 10^5 M_{\text{feed}}}{\rho \eta_{\text{pump}}}$$

where P_{feed} is the applied feed pressure in [bar], ρ is the density of the solution [kg/m^3] and η_{pump} is the efficiency of the high pressure pump [-].

The number of pressure vessels (i.e. the total membrane area available in the stage) can be fixed in the simulation or can be calculated, when a fixed recovery is required, as the ratio between the required total permeate flow rate and the calculated water flux. The model is able to simulate the RO plant when a certain feed pressure and a certain total membrane area are given as inputs and in this case the permeate flow rate and the plant recovery are calculated. More often, the recovery is given as the main requirement and the feed pressure is calculated as a consequence through an optimization tool. The resolution procedure is shown in Figure 5.

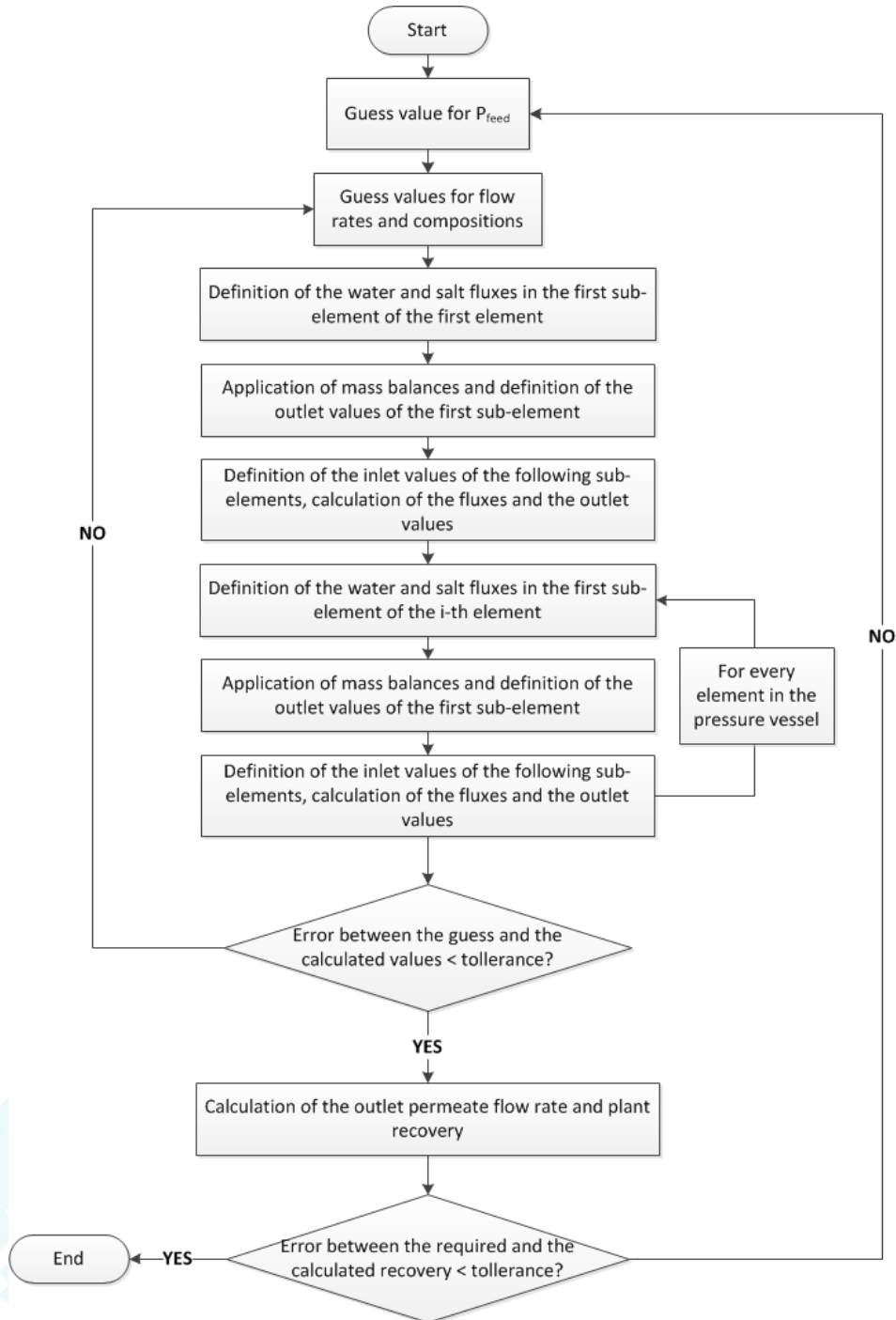


Figure 5: Resolution procedure of the RO plant model

The resolution of the multi-stage system is analogous and the permeate flow rate produced by the first stage is sent as the feed to the following stage.

5.4. RO Model Validation

Some charts are reported with reference to the validation performed through the comparison with the commercial software WAVE, developed by Dow (www.dow.com/water-and-process-solutions/resources/design-software). Some simulations were performed with a single stage RO plant at different recoveries. The main outputs compared are the required feed pressure and the average permeate water flux. The charts show a very good agreement between the model results and the results produced by Wave, ensuring a good reliability of the model.

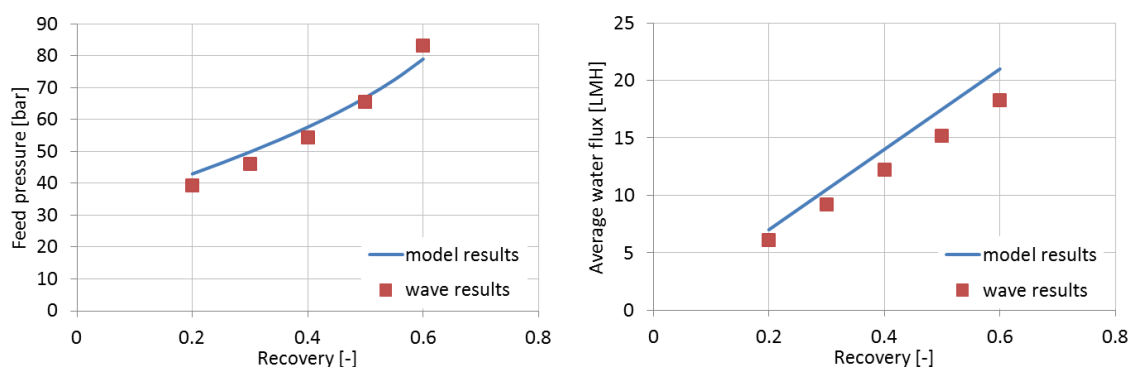


Figure 6: Validation charts: comparison between the feed pressure (on the left) and of the average permeate water flux (on the right) calculated by the model and the one calculated by WAVE software

5.5. RO Nomenclature

A_{membr}	pure water permeability in the membrane [kg/(s m ² bar)]
B_{membr}	solute permeability in the membrane [kg/(s m ²)]
F_w	water flux [kg/(s m ²)]
F_s	salt flux [kg/(s m ²)]
T	operating temperature [K]
ΔP	transmembrane pressure difference [bar]
X	concentration [ppm]
R_{salt}	salt rejection [%]
A	membrane active area [m]
C_{membr}	membrane constant for the temperature correction factor [K]
M	flow rate [kg/s]
n_{discr}	number of discretization intervals [-]
R_{el}	element recovery [%]
R_{plant}	plant recovery [%]
P_{feed}	feed pressure [bar]
P_{RO}	electric power consumption [W]

Subscripts

f,w feed side at the membrane interface

f	feed side
p	permeate side
feed	feed solution
conc	concentrate solution
perm	permeate solution
perm,out	permeate produced by the plant
perm,out elem	permeate produced by the RO element
w	water
s	salt
elem	discretization element

Greek letters

$\Delta\Pi$	transmembrane osmotic pressure difference [bar]
$\Delta\Phi$	relative variation of the flux with time [-]
ρ	density of the solution [kg/m^3]
η_{pump}	efficiency of the high pressure pump [-]

Acronyms

RO	reverse osmosis
TCF	temperature correction factor
MAF	membrane ageing factor
CPF	concentration polarization factor
NDP	net driving pressure [bar]

6. Nanofiltration Model

The NF model is developed on different scales, i.e. the lowest scale describes the mechanisms within the membranes, the medium scale is relevant to the NF element, while the high scale regards the whole NF plant, given by a certain amount of vessels in parallel, each one containing some NF elements in series. The schematic representation of the NF unit, as it is described in the model, is reported in Figure 7.

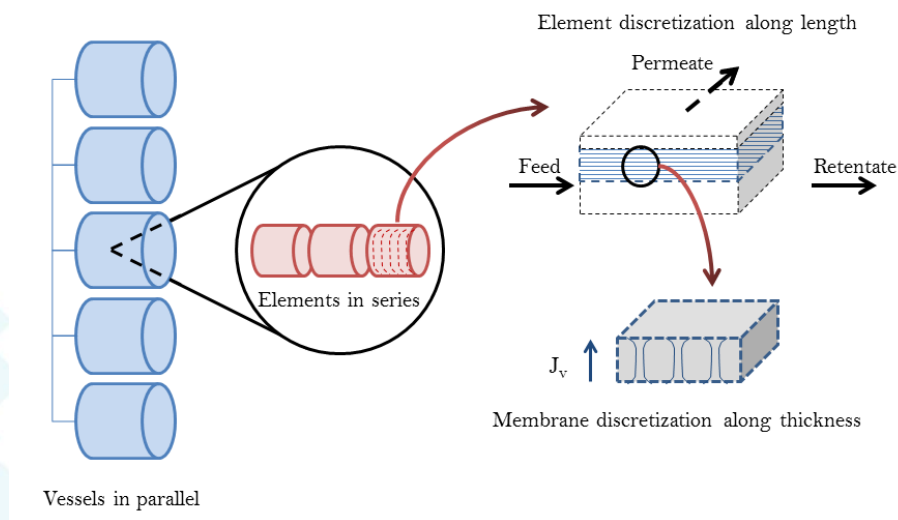


Figure 7: Different scales of modelling of the nanofiltration unit

6.1. DSMP-DE Membrane Model

Starting from the lowest scale, the mechanisms within the membranes are described via the Donnan Steric Partitioning Model with Dielectric Exclusion (DSMP-DE). In literature, there are numerous studies regarding the modelling of NF membranes and the DSMP model is the most widely used (Bowen et al. 1997, 2004, Geraldes and Alves 2008). The model allows a full characterization of the NF membrane, knowing four parameters, i.e.:

- the membrane pore radius (r_{pore})
- the active thickness (δ_m)
- the dielectric constant within the pores (ϵ_{pore}) and
- the fixed charge density (X_d).

These parameters are necessary for the estimation of the membrane rejection of a species i , being it defined as $1 - C_{pi} / C_{\text{feed}i}$. The system of equations composing the DSMP-DE model is linearized according to (Geraldes and Alves 2008) and solved in Python via the LAPACK routine `_gesv`, which is typically used to solve linear systems. The problem is then solved via iterations, updating the coefficients of the linearized equations and solving the linear system, until the residuals relevant to the imposed conditions are below a user-defined threshold ($<10^{-4}$).

The DSMP-DE model consists in the resolution of the extended Nernst-Planck equation along the thickness of the membrane, which takes into account the three different mechanisms of ion transport, i.e.:

- convection
- diffusion and
- electro-migration (Equation 6.1 in Table 8).

The main equations are reported in Table 8, where C_i^b , C_i^{bm} , $C_{i,j}^m$, and C_i^p represent the concentration of the species i in the bulk solution, at the bulk-membrane interface just before entering in the pore, in the j -th interval within the membrane, and in the permeate, respectively. J_i and J_v are the flux of the species i and the solvent (water) convective flux across the membrane. $K_{i,c}$, $k_{i,d}$ are the hindered convective and diffusive mass transfer coefficients of the ions within the pore, depending on λ , i.e. the ratio between the solute radius (r_i) and the pore radius (r_{pore}). $D_{i,p}$ is the diffusivity of the species i within the pore, which is corrected with respect to the diffusivity in the bulk via $k_{i,d}$. $K_{c,i}^{\text{bulk}}$ is the mass transfer coefficient in the bulk, depending on the flow regime, while $k_{c,i}^{\text{bulk}}$ is obtained multiplying the mass transfer coefficient by a factor depending on the permeation flux through the membrane (Geraldes and Afonso 2006).

Table 8: Equations of the implemented DSPM-DE model

(6.1)	$j_i = J_v C_{i,p} = -D_{i,p} \frac{C_{i,j+1}^m - C_{i,j}^m}{\delta y_j} - \frac{1}{2} z_i (C_{i,j+1}^m + C_{i,j}^m) D_{i,p} \frac{F}{RT} \frac{\psi_{j+1} - \psi_j}{\delta y_j} + \frac{1}{2} k_{i,c} (C_{i,j+1}^m + C_{i,j}^m) J_v$
(6.2)	$k_{i,d} = \frac{1 + \frac{9}{8} \lambda \ln(\lambda) - 1.56034 \lambda + 0.528155 \lambda^2 + 1.91521 \lambda^3 - 2.81903 \lambda^4}{+0.270788 \lambda^5 + 1.10115 \lambda^6 - 0.435933 \lambda^7} \Phi_i$
(6.3)	$k_{i,c} = \frac{1 + 3.867 \lambda - 1.907 \lambda^2 - 0.834 \lambda^3}{1 + 1.867 \lambda - 0.741 \lambda^2}$
(6.4)	$D_{i,p} = k_{i,d} D_{i,\infty}$
(6.5)	$\frac{\gamma_{i,1}^m C_{i,1}^m}{\gamma_{i,1}^{bm} C_{i,1}^{bm}} = \Phi_i \Phi_B \exp\left(-\frac{z_i F}{RT} \Delta \Psi_{D,bm}\right)$
(6.6)	$\frac{\gamma_{i,N}^m C_{i,N}^m}{\gamma_{i,N}^p C_{i,N}^p} = \Phi_i \Phi_B \exp\left(-\frac{z_i F}{RT} \Delta \Psi_{D,pm}\right)$
(6.7)	$\ln \gamma = -A z_i^2 \left(\frac{\sqrt{I}}{1 + \sqrt{I}} - 0.3 I \right)$
(6.8)	$A = \frac{e_0^3 N_A^{1/2}}{\ln(10) 4\pi \sqrt{2} (\epsilon k_B T)^{3/2}}$
(6.9)	$\Phi_B = \exp\left(-\frac{\Delta W_i}{k_B T}\right)$
(6.10)	$\Delta W_i = \frac{z_i^2 e_0^2}{8\pi \epsilon_0 r_i} \left(\frac{1}{\epsilon_{pore}} - \frac{1}{\epsilon_{bulk}} \right)$
(6.11)	$\Phi_i = (1 - \lambda_i)^2$
(6.12)	$\sum_i z_i C_i^{bm} = 0$
(6.13)	$\sum_i z_i C_i^p = 0$
(6.14)	$\sum_i z_i C_{i,j}^m + X_d = 0$
(6.15)	$j_i = -k_{c,i}^{bulk} (C_{i,1}^{bm} - C_{i,1}^b) + J_v C_{i,1}^{bm} - z_i C_{i,1}^{bm} D_{i,\infty} \frac{F}{RT} \xi$
(6.16)	$k_{c,i}^{bulk} = k_{c,i}^{bulk} \Xi = k_{c,i}^{bulk} \left[\frac{J_v}{k_{c,i}^{bulk}} + \left(1 + 0.26 \left(\frac{J_v}{k_{c,i}^{bulk}} \right)^{1.4} \right)^{-1.7} \right]$

The resolution provides the ion partitioning at the two membrane interfaces (equation 6.5 for the bulk-membrane interface and equation 6.6 for the permeate-membrane interface), which is determined by the Donnan equilibrium, the steric effect due to the sieving effect of the membrane (evaluated via the coefficient Φ_i , calculated via equation 6.11) and the dielectric exclusion (estimated through the coefficient Φ_B , i.e. the Born solvation contribution for partitioning, see equations 6.9-

6.10). This last effect was widely investigated in literature, since it has a prominent role in the definition of the ion rejection (Vezzani and Bandini 2002, Oatley et al. 2012). In fact, the dielectric exclusion is mainly due to the variation of the solvent dielectric properties inside the pores, caused by an alteration of the solvent structure. This different dielectric constant of the solvent inside the pores gives rise to a barrier to ion solvation, which constitutes an additional exclusion term. In the interface equilibrium, the concentrations are multiplied by the activity coefficient γ , to take into account the non-ideality of the solutions, estimated via the Davies equations (6.7-6.8). Other conditions which have to be fulfilled are the electroneutrality on the bulk and on the permeate side and inside the membrane, where a fixed charge density X_d is present (Equation 6.12, 6.13, 6.14 respectively). Finally, the mass transfer resistance on the bulk side is taken into account to calculate the concentration of the ions on the bulk-membrane interface (just before entering into the pore). Therefore, the balance in equation 6.15 represents the solute flux from the bulk to the membrane and it is used to estimate the role of the concentration polarization. This effect is neglected on the permeate side.

The mass transfer coefficient in the bulk is estimated via the correlation developed for spiral wound membranes, reported in equation 6.17 (Senthilmurugan et al. 2005).

$$(6.17) \quad k_{c,i}^{\text{bulk}} = 0.753 \left(\frac{\eta_{\text{mix}}}{2 - \eta_{\text{mix}}} \right)^{1/2} \left(\frac{D_{i,\infty}}{h_f} \right) Sc^{-1/6} \left(\frac{Pe_i h_f}{L_{\text{mix}}} \right)^{1/2}$$

where η_{mix} is the mixing efficiency of the spacer, h_f is the height of the feed channel, L_{mix} is the mixing length of the spacer, Pe and Sc are the Peclet and the Schmidt adimensional numbers respectively, i.e.

$$Pe = \frac{2 h_f u_w}{D_{i,\infty}} \text{ and } Sc = \frac{\eta}{\rho D_{i,\infty}}.$$

Finally, ψ represents the electric potential across the membrane, ξ the electric potential gradient at the bulk-membrane interface, outside the electric double layer, and $\Delta\psi_{\text{bm}}$ and $\Delta\psi_{\text{pm}}$ represent the potential difference at the bulk-membrane interface and at the permeate-membrane interface, respectively.

The solvent flux J_v through the membrane is estimated via Hagen-Poiseuille relation, depending on the membrane geometric parameters and on the net driving pressure:

$$(6.18) \quad J_v = \frac{\Delta P r_{\text{pore}}^2}{8 \eta \delta_m}$$

where η is the solution viscosity, δ_m is the active membrane thickness and ΔP is given by the difference between the pressure difference between bulk and permeate channel and the osmotic pressure $\Delta\Pi$, given by equation 6.19.

$$(6.19) \quad \Delta\Pi = RT \sum_i (C_i^{\text{bm}} - C_i^{\text{p}})$$

6.2. NF Element and Plant Model

The DSPM-DE model is integrated for the resolution of a whole NF element, discretizing the length of the membrane and applying mass balances to every interval. As shown by Roy et al. (Roy et al. 2015), also for a spiral wound element it is possible to apply a one-dimensional model, without significant errors, since the variation of the permeate concentration and flow rates along the width of the membrane is negligible. Consequently, an iterative one-dimensional model is employed, in which for every discretization interval the average value of the concentration, flow rates and pressure within the interval are accounted for the calculation of the osmotic pressure and the bulk mass transfer coefficient. The mass balances implemented to estimate the output concentrations and flow rates, together with the pressure losses definition along the element (Roy et al. 2015), are reported in Table 9.

Once the single element is modelled, to switch to an industrial NF plant scale, a certain number of elements are put in series inside a vessel. More in detail, the concentrate flow rate produced by one element is fed to the following element, while the produced permeates are finally mixed together. Moreover, typically, many pressure vessels are arranged in parallel to achieve a certain recovery rate ($M_{p,out} / M_{feed}$), which corresponds to a required permeate flow rate. Thus, for the overall plant resolution, an iterative calculation is set up, in which a guess number of vessels, i.e. a guess total membrane area, is given through the ratio between the required permeate flow rate and a guessed average solvent flow rate through the membrane. Thus, the series of elements is solved, the average solvent flux is recalculated in relation to the net driving pressure along the elements, and the total recovery rate is calculated. At this point, the number of pressure vessels is updated and the iterative calculation stops as soon as the overall recovery ratio is higher than or equal to the required one. This last iterative procedure needs only a few iterations but it is necessary, since the solvent flux through the membrane changes significantly along the membrane length and from one element to another and accounting only the flux at the first element entrance would lead to a strong underestimation of the required vessels, with important economic consequences.

Table 9: Equations to model a nanofiltration element

(6.20)	$M_p[x] = M_p[x - 1] + J_v[x] \frac{A_{membr,tot}}{n_{elem}n_{discr,L}}$
(6.21)	$M_{ret}[x] = M_b[x] - J_v[x] \frac{A_{membr,tot}}{n_{elem}n_{discr,L}}$
(6.22)	$C^p_i[x] = \frac{C^p_i[x - 1]M_p[x - 1] + j_i[x] \frac{A_{membr,tot}}{n_{elem}n_{discr,L}}}{M_p[x]}$
(6.23)	$C^{ret}_i[x] = \frac{C^b_i[x]M_b[x] - j_i[x] \frac{A_{membr,tot}}{n_{elem}n_{discr,L}}}{M_{ret}[x]}$
(6.24)	$M_b[x] = M_{ret}[x - 1]$
(6.25)	$C^b_i[x] = C^{ret}_i[x - 1]$

$$(6.26) \quad P[x] = P[x - 1] - \Delta P_{\text{losses}} = P[x - 1] - \frac{f}{2} \frac{dx}{D_H} \rho_w u_w^2$$

$$(6.27) \quad f = \frac{6.23}{\text{Re}^{0.3}}$$

where M_p and C_{pi} are the mass flow rate and the concentrations in the permeate channel, M_{conc} and C_{conci} are the flow rate and the concentrations in the concentrate channel, which are equal to the feed flow rate and the concentration of the feed in the next interval (M_b and C_{bi}). Regarding the pressure losses definition, f is the friction factor, dx is the length of the discretization interval, D_H is the hydraulic diameter relevant to the feed channel, employed also in the calculation of Re , and u_w is the feed velocity.

Finally, also in the case of the NF plant, the electric power requirement is calculated in analogy with the RO plant (Equation 5.22) and it is given by the power demand of the feed pump.

6.3. NF Model Validation

The DSPM-DE model was validated via the comparison with some experimental results reported in literature for two different salt solutions in presence of NF270 membranes (Oatley et al. 2012). The membrane parameters employed for the validation were taken equal to the ones taken in the reference work. As shown in Figure 8, there is a very good agreement between the experimental and the model results for both cases.

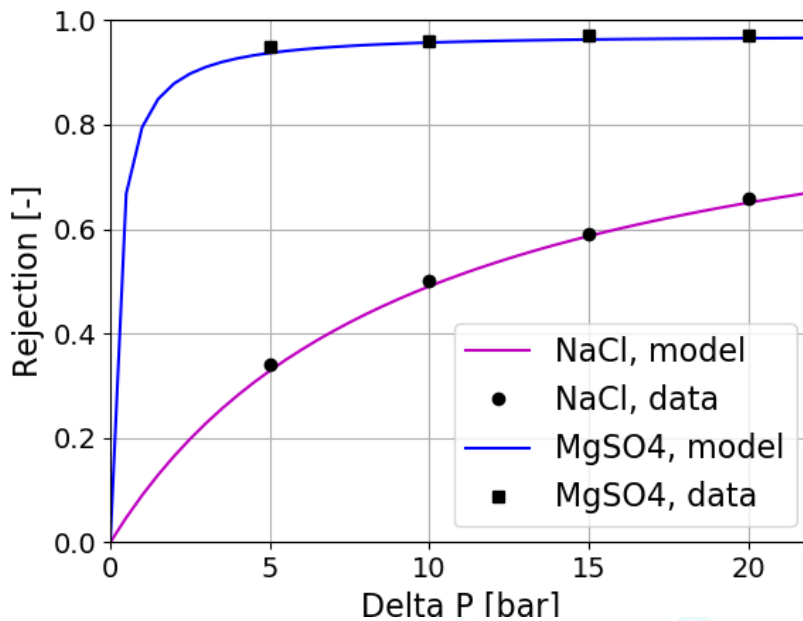


Figure 8: Rejection experimental values (black dots) (Oatley et al. 2012) and trend simulated by the model in presence of NaCl or MgSO4 with NF270 membranes

6.4. NF Nomenclature

J_v water flux through the NF membrane [m/s]

r_{pore}	NF membrane pore radius [nm]
X_d	NF membrane charge density [mol/m ³]
r_i	ion radius [nm]
C	concentration [mol/m ³]
x	direction of the feed flow in the NF element
y	direction across the membrane from the feed to the permeate side
M	flow rate [m ³ /s]
j_i	flux of the ion i [m/s]
$A_{\text{membr,tot}}$	total membrane area for each vessel (6 elements with a area of 1x1m ²) [m ²]
n_{elem}	number of elements in each vessel
$n_{\text{discr,L}}$	number of discretization intervals along the NF element length
n_{vessel}	number of vessels in parallel
P	pressure [bar]
ΔP_{losses}	pressure losses along the element [bar]
ΔP	net driving pressure [bar]
f	friction factor [-]
dx	length of the discretization interval [m]
D_H	hydraulic diameter relevant to the feed channel [m]
Re	Reynolds number
Pe	Peclet number
Sc	Schmidt number
u_w	feed velocity [m/s]
$k_{i,c}$	hindered convective mass transfer coefficients of the ions within the pore
$k_{i,d}$	hindered diffusive mass transfer coefficients of the ions within the pore
$D_{i,p}$	diffusivity of the species i within the pore [m ² /s]
$D_{i,\infty}$	diffusivity of the species i in the bulk [m ² /s]
$k_{c,i}^{\text{bulk}}$	mass transfer coefficient in the bulk [m/s]
$k_{c,i}^{\text{bulk}}$	corrected mass transfer coefficient in the bulk [m/s]
z	ion valence
F	Faraday constant (9.64867 x 10 ⁴ C/eq)
R	ideal gas constant (8.314 J/(K mol))
T	Temperature [K]
N_A	Avogadro number (6.023 x 10 ²³ mol ⁻¹)
k_B	Boltzmann constant (1.38066 x 10 ⁻²³ J/K)
e_0	electronic charge (1.602 x 10 ⁻¹⁹ C)
A	temperature correction factor for the activity coefficient
I	ionic strength [mol/l]
h_f	height of the NF feed channel [m]
L_{mix}	mixing length of the spacer [m]

Greek letters

δ_m	NF membrane active layer thickness [μm]
ϵ_{pore}	dielectric constant within the pore
ϵ_{bulk}	dielectric constant in the bulk
ϵ_0	vacuum permittivity (8.854 x 10 ⁻¹² F/m)
ϵ	medium permittivity [F/m]
$\Delta\Pi$	osmotic pressure [bar]
ρ_w	solvent density [kg/m ³]
γ	activity coefficient
η	solution viscosity [Pa s]
λ	ratio between the solute radius and the pore radius
ψ	electric potential across the membrane [V]

ξ	electric potential gradient at the bulk-membrane interface [V]
$\Delta\psi_{D,bm}$	Donnan potential difference at the bulk-membrane interface [V]
$\Delta\psi_{D,pm}$	Donnan potential difference at the permeate-membrane interface [V]
Φ_i	steric coefficient
Φ_B	Born solvation contribution for partitioning
η_{mix}	mixing efficiency of the spacer
ΔW	Born solvation energy barrier [J]
ξ	correction factor for the mass transfer coefficient

Subscripts and superscripts

i	ion index
j	index for the discretization within the membrane thickness
p	NF permeate along the NF element
ret	NF retentate along the element
m	inside the membrane
feed	solution entering into the element
out	outlet of the NF unit
b	solution entering into the interval along the NF element
bm	bulk-membrane interface

Acronyms

TVC	Thermo-vapor compressor
NF	Nanofiltration
DSPM-DE	Donnan Steric Partitioning Model with Dielectric Exclusion

7. Crystallizer Model

In literature, there are many studies related to the recovery of magnesium from brines, reporting several experimental campaigns aiming at controlling the purity and the crystals size distribution of precipitate particles (Turek and Gnot 1995, Liu et al. 2011, Cipollina et al. 2014). However, only a few works in literature are devoted to modelling the crystallization of $Mg(OH)_2$. With this regard, a fundamental work was carried out by Alamdari et al. (Alamdari et al. 2008), in which the kinetics of secondary nucleation, growth and agglomeration were estimated via the fitting of experimental data obtained for a batch and a semi-batch seeded reactor.

Generally speaking, the crystallization is modelled via population balance equations, which are able to describe the properties of the particles in space and time. The population balance equation takes into account the different mechanisms occurring inside the crystallizer, i.e. nucleation, growth and aggregation, estimating the variation of the number density function $n(L, t)$, according to the following expression (Omar and Rohani 2017):

$$(7.1) \quad \frac{\partial n(L, t)}{\partial t} = -\frac{\partial [G(L) n(L, t)]}{\partial L} + B(L, t) - D(L, t)$$

where L is the particle length, $G(L)$ is the growth rate, $B(L, t)$ is the birth rate due to the aggregation and $D(L, t)$ is the death rate due to the aggregation. In this case, the breakage of the crystals is neglected.

The population balance equation can be solved following different approaches; one of the most widely used involves the conversion of the population balance into a moment balance. In particular,

an attractive option is the quadrature method of moments (QMOM), which is robust and able to handle complex systems, including aggregation and breakage mechanisms (Marchisio et al. 2003b). This method is based on a quadrature approximation, which changes the integral in the moments' definition into a summation.

$$(7.2) \quad m_k = \int_0^{+\infty} n(L)L^k dL \sim \sum_{i=1}^{N_q} w_i L_i^k$$

where N_q is the number of quadratures ($N_q=3$ was shown to be sufficient to describe the moments evolution accurately), w_i are the weights and L_i are the abscissas. The calculation of weights and abscissas is performed via the product-difference algorithm, for which it is necessary to know the first $2N_q$ moments. Thus, to follow the evolution of the moments with time, starting from a known set of the first six orders moments at t_0 , it is possible to apply the balance of the moments, taking into account the occurring mechanisms, to calculate the moments at t_1 . These moments are, then, employed to calculate the weights and the abscissas via the product-difference algorithm, which are useful to estimate the kinetics at t_1 .

For the time being, the attention is focused on the balances on the third moment, which is a measure of the mass of precipitated crystals (M_T).

To this aim, the primary and secondary nucleation kinetics, together with the growth rate, were accounted for the estimation of the M_T variation. The agglomeration kernel was not included, since it does not influence the total mass of crystals but only the crystal size (Marchisio et al. 2003a). The secondary nucleation and growth kinetics are function of the system supersaturation and of M_T , according to the expression given by Alamdari. However, the secondary nucleation depends on the supersaturation with an exponent (b in equation 7.5) equal to 2, instead of 3 as found by Alamdari. This is due to a fundamental difference between the two systems arrangement, which leads to a much higher supersaturation in the system under investigation.

Table 10: Crystallization kinetics and precipitated crystal mass balance

(7.3)	$S = \frac{[Mg^{++}][OH^-] - K_{sp,Mg(OH)_2}}{K_{sp,Mg(OH)_2}}$
(7.4)	$N_{prim} = k_{prim} \exp\left(-\frac{16\pi v^2}{3 k_B^3 T^3} \frac{\sigma^3}{(\ln S)^2}\right)$
(7.5)	$N_{sec} = k_{sec} S^b M_T$
(7.6)	$G_v = 3k_g k_v^{1/3} S g_v^{2/3} 10^{-6}$
(7.7)	$\frac{dM_T}{dt}_{nucl} = (N_{prim} \rho_{solv} + N_{sec} \rho_{sol}) dV \rho_{cryst} v_{nucl} 10^6$
(7.8)	$\frac{dM_T}{dt}_{growth} = G_v \rho_{cryst}$

$$(7.9) \quad \frac{dM_T}{dt}_{tot} = \frac{dM_T}{dt}_{nucl} + \frac{dM_T}{dt}_{growth}$$

where $K_{sp, Mg(OH)_2}$ is the solubility product of $Mg(OH)_2$. N_{prim} [$\#/(g_{sol} s)$], N_{sec} [$\#/(g_{sol} s)$] and G_v [cm^3/s] are the primary nucleation, secondary nucleation and volume-based growth rate, respectively. In equation 7.4, k_{prim} is assumed to be equal to 12 [$\#/(g_{sol} s)$], on the basis of experimental data, v is the volume of one solute molecule [m^3] and σ is the crystal solution interfacial energy, equal to 0.123 J/ m^2 for $Mg(OH)_2$. In equations 7.5 and 7.6, k_{sec} is equal to 0.418 [$\#/(g_{cryst} s)$], k_g is $2.13 \cdot 10^{-11}$ [m/s], k_v is the volume shape factor of the particle and \bar{v} is the average particle size [m^3]. Finally, v_{nucl} is the minimum particle size and $(dM_T/dt)_{nucl}$, $(dM_T/dt)_{growth}$ and $(dM_T/dt)_{tot}$ are the measure of the increase of the mass of precipitated crystals due to nucleation, growth and total in [g_{cryst}/s].

Different possible crystallizer reactors may be used, for example a batch crystallizer is typically used also at the industrial scale but mostly for small production volumes. In this case, a plug-flow arrangement with different alkaline solution injections was selected, in order to be able to deal with higher volumetric flow rates and to avoid too high supersaturations. The length of the reactor was divided into different elements, as many as the injections and each element was discretized into n intervals. Two discretization steps are employed for each element, since the extremely high supersaturation occurring at the NaOH-solution inlet made necessary to apply a very narrow discretization step ($10^{-6}m$), while after the supersaturation fall a discretization step of $10^{-2}m$ was accounted. In the first interval of each element the total flow rate was increased by the corresponding entering NaOH solution, while, in the rest of the element, the flow rate was constant. The schematic representation of the analyzed system is reported in Figure 9.

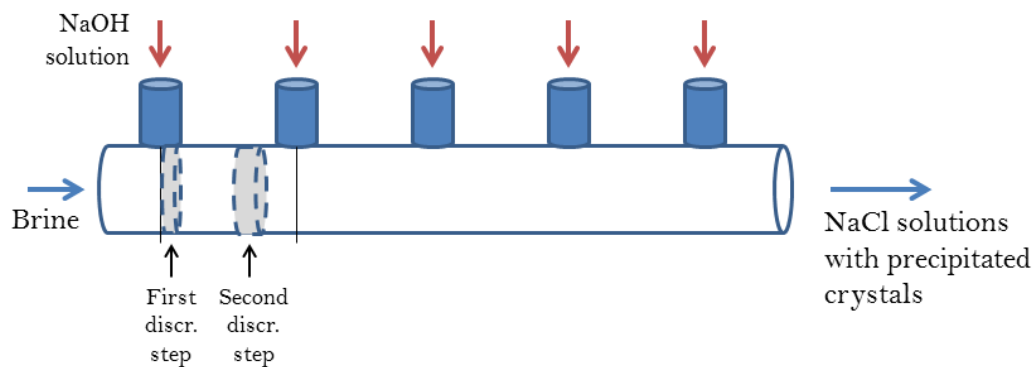


Figure 9: Schematic representation of the plug-flow reactor used for the crystallization step.

For each interval, the kinetics and the M_T generation speed were estimated and used for the evaluation of the concentration of Mg^{++} and OH^- , as shown in the equations 7.10 and 7.11. In equation 7.12, the balance on the OH^- concentration in the first interval of each element is reported,

while the balance on the Mg^{++} concentration does not change. Finally, since the reactor is unseeded, in the first interval of the first element only the primary nucleation has to be accounted.

$$(7.10) \quad [Mg^{++}][x] = \frac{Q_{brine}[x-1][Mg^{++}][x-1] 10^{-3} - \frac{dM_T}{dt}_{tot} \frac{60}{MW_{Mg(OH)_2}}}{Q_{brine}[x]10^{-3}}$$

$$(7.11) \quad [OH^-][x] = \frac{Q_{brine}[x-1][OH^-][x-1] 10^{-3} - 2 \frac{dM_T}{dt}_{tot} \frac{60}{MW_{Mg(OH)_2}}}{Q_{brine}[x]10^{-3}}$$

$$(7.12) \quad [OH^-][x] = \frac{Q_{NaOH}[OH^-]_{in} 10^{-3} + Q_{brine}[x-1][OH^-][x-1] 10^{-3} - 2 \frac{dM_T}{dt}_{tot} \frac{60}{MW_{Mg(OH)_2}}}{Q_{brine}[x]10^{-3}}$$

where Q_{brine} is the flow rate proceeding along the reactor in [ml/min], Q_{NaOH} is the flow rate of alkaline solution for each injection and $[OH^-]_{in}$ is its concentration in [mol/l]. Finally, $[Mg^{++}]$ and $[OH^-]$ are the concentration in the brine along the reactor in [mol/l].

However, because of the very low solubility of the two hydroxides, it is generally observed that a conversion of 100% occurs in the reactors. For this reason, for the first simulations of the $Mg(OH)_2$ and $Ca(OH)_2$ crystallizers, a conversion of 100% was assumed in both reactors. Consequently, trivial mass balances were implemented to convert the total inlet molar flow rate of Mg^{++} and Ca^{++} into an outlet molar flow rate of $Mg(OH)_2$ and $Ca(OH)_2$. The other relevant calculation, also performed via mass balances, regards the alkaline solution flow rate required for the two separation stages. The required molar flow rate is estimated multiplying the entering molar flow rates of Mg^{++} and Ca^{++} , coming from the nanofiltration, by the stoichiometric coefficient (i.e. 2) and considering an excess defined through mass balances, which allows reaching a pH equal to 13. The volume flow rate is estimated assuming a concentration of the NaOH solution equal to 1 mol/l.

7.1. Crystallizer Nomenclature

L	particle length [m]
G(L)	growth rate
B(L, t)	birth rate
D(L, t)	death rate
N_q	number of quadratures
w_i	weights
L_i	abscissas
M_T	mass of precipitated crystals [g]
$K_{sp, Mg(OH)_2}$	solubility product of $Mg(OH)_2$
N_{prim}	primary nucleation rate [$\#/(g_{solv} s)$]
N_{sec}	secondary nucleation rate [$\#/(g_{sol} s)$]
G_v	volume-based growth rate [cm^3/s]
k_v	volume shape factor of the particle [-]
v	average particle size [m^3]
v_{nucl}	minimum particle size [m^3]

Q_{brine}	flow rate proceeding along the reactor [ml/min]
Q_{NaOH}	flow rate of alkaline solution for each injection [ml/min]
$[\text{OH}^-]_{\text{in}}$	NaOH concentration in the alkaline solution [mol/l]
$[\text{Mg}^{++}]$	concentration of Mg^{++} in the brine [mol/l]
$[\text{OH}^-]$	concentration of OH^- in the brine [mol/l]

8. Membrane Distillation Model

Membrane Distillation is a separation process, which makes use of a microporous hydrophobic membrane, permeable only to the water vapor. The driving force of the separation mechanism is the vapor pressure difference, given by a temperature difference, at the two membrane interfaces. This driving force leads to a net water flux, in the vapor phase within the pores, from the hot channel, where the feed solution flows, to the cold channel, where the permeate solution flows. In the last years, the MD process has been subject of several studies in literature, because of its high potentialities for desalination: for example, it requires lower temperatures and smaller footprint than the Multi-Effect Distillation plants, it is very suitable in the case of low-grade waste heat availability and it works at much lower pressures than the Reverse Osmosis. Moreover, since the separation occurs by evaporation of water at the hot interface and by condensation of the vapor at the cold interface, theoretically, the rejection to any solute is 100% (Al-Obaidani et al. 2008). The main issue of the MD process regards a non-ideality phenomenon, namely the temperature polarization. Therefore, the driving force for the vapor flux depends on the temperature difference at the two interfaces ($T_{\text{membrane,hot}} - T_{\text{membrane,cold}}$) and these temperatures are different from those relevant to the bulk side, because of the temperature polarization phenomenon (Qtaishat et al. 2008). Another drawback of the MD process is that the water flux is relatively low, if compared with other technologies as RO, and the heat lost by conduction is significant, thus the thermal energy requirement is typically very high (Alkhudhiri et al. 2012). Several configurations of the MD unit have been proposed in order to reduce these drawbacks: the most widely used configuration is the Direct Contact MD (DCMD), where both hot and cold fluids are in direct contact with the membrane on the two sides; other configurations present an air gap between the membrane and a cold condensing plate (AGMD) or a cold sweep gas which substitute the cold permeate and provides the driving force (SGMD) or the vacuum applied on the permeate side to enhance the pressure difference (VMD). These configurations are schematically represented in Figure 10.

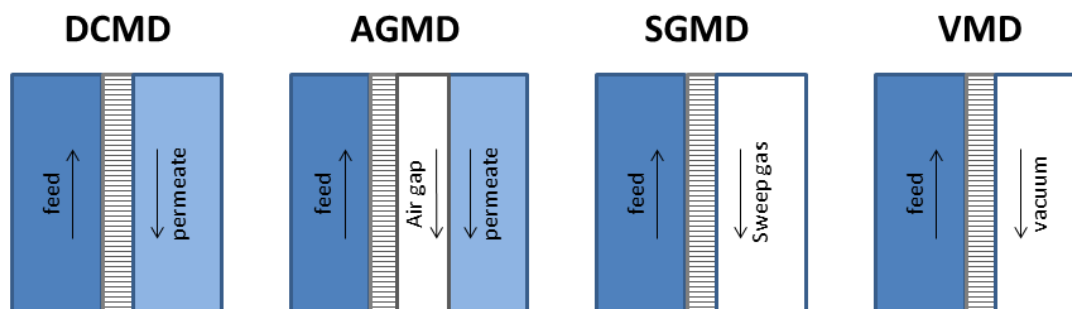


Figure 10: Schematic representation of some of the most widely used MD configurations.

All these configurations have advantages and disadvantages, for example the AGMD ensures a higher heat recovery but the mass transfer is limited by the air gap, or the VMD has negligible heat losses and high fluxes but the electric consumption increases sharply for the vacuum pump (Eykens et al. 2016). Overall, even if the DCMD reports high heat losses for conduction, it was chosen for the present work because of its operational simplicity, the possibility to operate in any configuration (e.g. flat sheet or spiral wound) and its high flux (Al-Obaidani et al. 2008).

8.1. DCMD Element Model – Heat and Mass Transfer

Firstly, the DCMD element was modelled through the description of the heat and mass transfer in the channels and across the membranes. The system presents a single membrane, which is in contact with a hot fluid (feed) on one side and with a cold fluid (permeates) on the other side, as shown in Figure 11. The membrane presents micro pores, which cross the whole thickness of the membrane and at both ends of the pores a liquid/vapor interface is generated. Different heat and mass transport mechanisms are involved: a convective heat and mass flux from the feed bulk to the feed-membrane interface and from the permeate-membrane interface to the permeate bulk, a conductive heat flux within the pores and the vapor diffusion through the pores, which is coupled with the latent heat transport. The combination of these mechanisms gives rise to a temperature profile from the feed bulk to the permeate bulk, where the temperature polarization effect is evident, i.e. the temperature at the bulk membrane interface ($T_{m,hot}$) is lower than the temperature in the bulk ($T_{bulk,hot}$) and the temperature at the permeate membrane interface ($T_{m,cold}$) is higher than the temperature in the permeate bulk ($T_{bulk,cold}$). Also in the concentration profile, a similar effect is noticed, namely the concentration polarization effect, which leads to a concentration at the bulk membrane interface higher than the one in the bulk. These two phenomena are detrimental for the water flux, since they both contribute to the decrease of the driving force across the membrane.

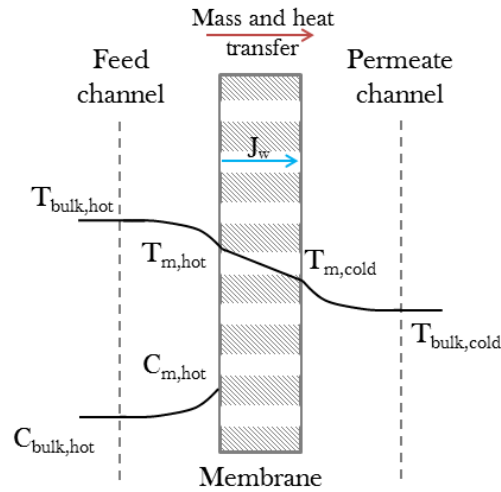


Figure 11: Representation of the DCMD element with the temperature and concentration profile

8.1.1. Heat Transfer

For what concern the heat transfer, this accounts for different terms: the convective heat flux from the feed bulk to the feed-membrane interface ($Q_{conv,hot}$), the total heat flux through the membranes, i.e. the sum of the conductive flux ($Q_{cond,m}$) and the latent heat transferred with the vapor flux ($Q_{evap,m}$), and the convective heat flux from the permeate-membrane interface to the permeate bulk ($Q_{conv,cold}$). For the conservation of energy under steady-state conditions, these three heat fluxes have to be equal (Khalifa et al. 2017). The definition of the heat fluxes is reported in equation (8.1-8.5).

$$(8.1) \quad Q_{conv,hot} = h_f(T_{bulk,hot} - T_{m,hot})$$

$$(8.2) \quad Q_m = Q_{cond,m} + Q_{evap,m}$$

$$(8.3) \quad Q_{cond,m} = h_m(T_{m,hot} - T_{m,cold})$$

$$(8.4) \quad Q_{evap,m} = J_w \Delta H_{evap} \left[\frac{T_{m,hot} + T_{m,cold}}{2} \right]$$

$$(8.5) \quad Q_{conv,cold} = h_p(T_{m,cold} - T_{bulk,cold})$$

where h_f , h_m and h_p are the heat transfer coefficients in the hot channel, in the membrane and in the cold channel, respectively [$W/(m^2 K)$]. J_w is the water flux through the membrane [$kg/(m^2 s)$] and ΔH_{evap} is the latent heat of vaporization of water [J/kg], calculated at the average temperature inside the membrane.

From the equality of the heat fluxes, it is possible to calculate directly the temperature at the bulk membrane interface and at the permeate membrane interface, according to the following equations (Khayet et al. 2004):

$$(8.6) \quad T_{m,hot} = \frac{\frac{k_m}{\delta_m} \left(T_{b,cold} + \frac{h_f}{h_p} T_{b,hot} \right) + h_f T_{b,hot} + J_w \Delta H_{evap}}{\frac{k_m}{\delta_m} + h_f + k_m \frac{h_f}{h_p \delta_m}}$$

$$(8.7) \quad T_{m,cold} = \frac{\frac{k_m}{\delta_m} \left(T_{b,hot} + \frac{h_p}{h_f} T_{b,cold} \right) + h_p T_{b,cold} + J_w \Delta H_{evap}}{\frac{k_m}{\delta_m} + h_p + k_m \frac{h_p}{h_f \delta_m}}$$

where k_m is the membrane conductivity [W/(m K)] and δ_m is the membrane thickness [m]. The membrane conductivity is calculated combining the conductivity of air (k_{air}) and the conductivity of the polymeric structure ($k_{membr,pol}$) through the membrane porosity ε , according to the following equation:

$$(8.8) \quad k_m = \varepsilon k_{air} + (1 - \varepsilon) k_{membr,pol}$$

The heat transfer coefficients in the hot and in the cold channel (h_f and h_p) are estimated starting from the Nusselt number, according to the equation:

$$(8.9) \quad h = \frac{Nu \, k}{D_h}$$

where D_h is the hydraulic diameter of the channel and k is the thermal conductivity of the fluid. Several correlations are reported in literature for the calculation of the Nusselt number as function of the Reynolds and the Prandtl number and for the two flow regimes (typically laminar if $Re < 2,300$ and turbulent if $Re > 2,300$). These correlations are also dependent on the specific system geometry, which is represented through the hydraulic diameter of the channel. Re and Pr numbers are defined as follows:

$$(8.10) \quad Re = \frac{\rho \, v D_h}{\mu}$$

$$(8.11) \quad Pr = \frac{C_p \, \mu}{k}$$

where μ is the dynamic viscosity of the fluid, v is the fluid velocity in the channel and C_p is the fluid specific heat. Some of these correlations are reported in the table below, where L is the channel length. Among these correlations, in the present work, the equations 8.12 and 8.17 have been used in presence of laminar or turbulent flow respectively, for both channels. This selection was performed on the basis of the validation of the model through the comparison with the experimental results reported by Hitsov et al. (Hitsov et al. 2017, 2018).

Table 11: Literature correlations for the estimation of Nu number in the feed and permeate channels

(8.12)	$Nu = 0.13 \, Re^{0.64} Pr^{0.38}$	Laminar flow (Andrjesdottir et al. 2013)
--------	------------------------------------	--

(8.13)	$Nu = 1.86 \left(\frac{Re Pr D_h}{L} \right)^{0.33}$	Laminar flow (Khalifa et al. 2017)
(8.14)	$Nu = 0.036 Re^{0.8} Pr^{1/3}$	Turbulent flow (Andrjesdottir et al. 2013)
(8.15)	$Nu = 0.027 Re^{0.8} Pr^{0.4} \left(\frac{\mu_{b,hot}}{\mu_{membr,hot}} \right)^{0.14}$	Turbulent flow, hot channel (Qtaishat et al. 2008)
(8.16)	$Nu = 0.027 Re^{0.8} Pr^{0.33} \left(\frac{\mu_{b,cold}}{\mu_{membr,cold}} \right)^{0.14}$	Turbulent flow, cold channel (Qtaishat et al. 2008)
(8.17)	$Nu = 0.22 Re^{0.69} Pr_{bulk}^{0.13} \left(\frac{Pr_{bulk}}{Pr_{membr}} \right)^{0.25}$	Turbulent flow (Hitsov et al. 2017)

8.1.2. Mass Transfer

In DCMD, the water flux through the membrane pores is typically expressed through a linear dependence on the driving pressure difference:

$$(8.18) \quad J_w = B_m (P_{m,hot} - P_{m,cold})$$

where B_m is the mass transfer coefficient [$kg / (m^2 s Pa)$], while $P_{m,hot}$ and $P_{m,cold}$ are the vapor pressures at the temperatures $T_{m,hot}$ and $T_{m,cold}$ respectively, calculated using the Antoine equation (Qtaishat et al. 2008). $P_{m,hot}$ is obtained multiplying the vapor pressure at $T_{m,hot}$ by the water activity at the concentration of the solution at the bulk membrane interface $C_{m,hot}$. The calculation of B_m is a widely discussed topic in literature and it is based on the definition of the main transport mechanisms through porous membranes, i.e. Knudsen diffusion, molecular diffusion or a combination of these two. The identification of the predominant mass transfer mechanism is possible through the calculation of the Knudsen coefficient, given by the ratio of the molecular mean free path within the pores and the pore diameter (λ/d_p). The definition of the molecular free path is reported in equation 8.19, where K_b is the Boltzmann constant, T and P_{pore} are the average temperature [K] and pressure [Pa] within the pores and d_{wat} is the collision diameter of water vapor molecules, assumed as hard spheres and equal to 2.64×10^{-10} m.

$$(8.19) \quad \lambda = \frac{K_b T}{\sqrt{2} \pi P_{pore} d_{wat}^2}$$

If the molecular mean free path is higher than the pore diameter ($Kn > 1$), the collisions between the molecules and the wall are dominant with respect to the collisions molecules-molecules, which means that the Knudsen diffusion is the most representative transport mechanism (Qtaishat et al. 2008). Conversely, if the pore diameter is higher than the molecular mean free path ($Kn < 0.01$) the predominant transport mechanism is the molecular diffusion. In most cases, the value of Kn is

between 0.01 and 1, which means that the transport is given by the combination of the two mechanisms. The definition of the mass transfer coefficient will then take into account both transport terms, here represented by $D_{w,k}$ and $D_{w,m}$, i.e. the Knudsen diffusion coefficient and the molecular diffusion coefficient respectively (Andrjesdottir et al. 2013).

$$(8.20) \quad D_{w,k} = \frac{2 r_{\text{pore}} \varepsilon}{3 \tau} \sqrt{\frac{8 R T}{\pi M_{w,\text{wat}}}}$$

$$(8.21) \quad D_{w,m} = 4.46 E - 6 \frac{\varepsilon}{\tau} T^{2.334}$$

$$(8.22) \quad B_m = \frac{1}{R T} \frac{D_{w,k} D_{w,m}}{D_{w,m} + P_{\text{air}} D_{w,k}} \frac{M_{w,\text{wat}}}{\delta_m}$$

where r_{pore} is the pore radius, τ is the membrane tortuosity, R is the universal gas constant, T is the average temperature within the pore [K], $M_{w,\text{wat}}$ is the molecular weight of water [kg/mol] and P_{air} is the air pressure inside the pores, calculated as the difference between the pressure in the pores (1.103E5 Pa) and the vapor pressure at the average temperature (Khalifa et al. 2017).

Finally, as already mentioned, the concentration polarization effect is usually accounted for the calculation of the concentration at the bulk membrane interface:

$$(8.23) \quad C_{m,\text{hot}} = C_{\text{bulk,hot}} e^{\frac{J_w}{k_{f,\text{mass}} \rho}}$$

where $k_{f,\text{mass}}$ is the mass transfer coefficient in the feed channel, calculated as:

$$(8.24) \quad k_{f,\text{mass}} = \frac{\text{Sh} D_{\text{NaCl,wat}}}{D_h}$$

where $D_{\text{NaCl,wat}}$ is the diffusivity of NaCl in water and Sh is the Sherwood number which is calculated in analogy with Nu number (Hitsov et al. 2017), as function of Re and Schmidt number:

$$(8.25) \quad \text{Sc} = \frac{\mu}{\rho D_{\text{NaCl,wat}}}$$

$$(8.26) \quad \text{Sh} = 0.22 \text{Re}^{0.69} \text{Sc}_{\text{bulk}}^{0.13} \left(\frac{\text{Sc}_{\text{bulk}}}{\text{Sc}_{\text{membr}}} \right)^{0.25}$$

The equations describing the mass and heat transfer were implemented on Python and solved following an iterative resolution procedure, which updates the temperature and feed concentration values at the bulk-membrane interface, until the difference between the three heat fluxes ($Q_{\text{conv,hot}}$, Q_m and $Q_{\text{conv,cold}}$) is minimized.

8.2. DCMD Unit Model – Mass and Energy Balances

The model described in the previous paragraph concerning the mass and heat transport mechanisms across the membrane has been scaled up, in order to simulate the whole DCMD unit. The unit is supposed to work in a counter-current mode, as shown in Figure 12, which makes necessary the implementation of an iterative procedure. Therefore, the MD unit was divided into a certain number of elements (usually 10, in literature also 3 or 5 elements are used (Hitsov et al. 2017)) and for each element the model relevant to the calculation of heat and mass transfer across the channels and the membrane was applied. Then, the elements were interconnected via the application of mass and energy balances, to calculate the inlet flow rates, temperatures and feed composition for any element. These balances are reported in the equations (8.27-8.31).

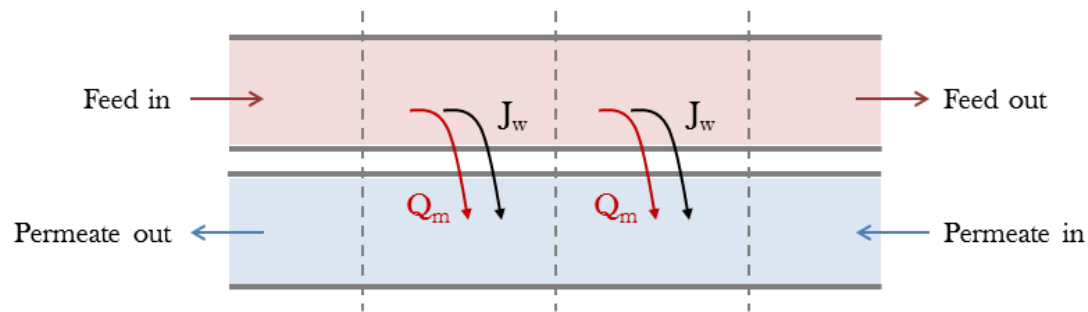


Figure 12: Schematic representation of a counter-current flat sheet DCMD unit

$$(8.27) \quad m_{f,out} = m_{f,in} - J_w A_{elem} 10^{-3}$$

$$(8.28) \quad m_{p,in} = m_{p,out} - J_w A_{elem} 10^{-3}$$

$$(8.29) \quad T_{f,out} = \frac{m_{f,in} C_{p,f,in} \rho_{f,in} T_{f,in} - Q_m A_{elem}}{m_{f,out} C_{p,f,out} \rho_{f,out}}$$

$$(8.30) \quad T_{p,in} = \frac{m_{p,out} C_{p,p,out} \rho_{p,out} T_{p,out} - Q_m A_{elem}}{m_{f,in} C_{p,f,in} \rho_{f,in}}$$

$$(8.31) \quad C_{f,out} = \frac{m_{f,in} \rho_{f,in} C_{f,in}}{m_{f,out} \rho_{f,out}}$$

The calculation starts giving the input values, relevant to the unit geometry, the membrane properties, the feed composition, flow rate and pressure and the permeate flow rate. Then, guess values of the temperature profiles (T_{bulk} and T_m) in the feed and in the permeate channel, of the feed and permeate flow rate profiles and of the feed concentration profile along the unit have to be provided. At this point, the first iteration runs assuming these guess values and solving the membrane model for every element and the mass balances between the elements. All the profiles are recalculated and the inlet flow rate and temperature of the permeate solution, which enters in

concerns the inlet feed concentration, which is increasing from one module to the following. For this reason, the calculation of the required number of modules in series is performed considering the water flux produced in the MD module at the average concentration between the feed inlet and the required outlet concentrations. The overall plant mass balances and the calculation of the required number of modules are reported in equations (8.31-8.34).

$$(8.32) \quad M_{\text{brine,plant}} = \frac{M_{\text{feed,plant}} C_{\text{feed}}}{C_{\text{brine,plant}}}$$

$$(8.33) \quad M_{\text{dist,plant}} = M_{\text{feed,plant}} - M_{\text{brine,plant}}$$

$$(8.34) \quad N_{\text{parallel}} = \text{int} \left(\frac{M_{\text{feed,plant}} \rho_{\text{feed,plant}}}{M_{\text{feed,in-design-lh}} \times 1000} \right)$$

$$(8.35) \quad N_{\text{tot,modules}} = \text{int} \left(\frac{M_{\text{dist,plant}}}{J_{\text{w,aver}} A_{\text{module}} 3600} \right)$$

Where $M_{\text{feed,plant}}$ is the total feed flow rate to be processed in [kg/h]; $M_{\text{brine,plant}}$ and $M_{\text{dist,plant}}$ are the concentrate and distillate flow rates, respectively, which have to be produced in the plant [kg/h]; $C_{\text{brine,plant}}$ is the required outlet concentration of the concentrate solution [ppm] and $J_{\text{w,aver}}$ is the average water flux in [kg/(m² s)], calculated at the average concentration between C_{feed} and $C_{\text{brine,plant}}$.

Finally, the electric and thermal energy requirements are estimated according to equations (8.36-8.40). Regarding the thermal energy requirement, firstly, the thermal energy required to heat the total feed flow rate up to the inlet hot temperature is calculated. Then, between each module and the following in the series, a heat exchanger for heat recovery from the permeate to the concentrate flow rate is accounted, with a minimum temperature difference of 10°C. The remaining heating and cooling requirements are calculated separately.

$$(8.36) \quad P_{\text{electric,pumps}} = \frac{2 N_{\text{tot,modules}} M_{\text{feed,in-design-lh}} \Delta P_{\text{in}}}{\eta_{\text{pump}} \times 1000 \times 3600}$$

$$(8.37) \quad P_{\text{thermal,feed}} = \frac{M_{\text{feed,plant}}}{3600} C_{\text{p,feed}} (T_{\text{feed,in}} - T_{\text{intake}})$$

$$(8.38) \quad P_{\text{thermal,heater}} = \frac{M_{\text{feed,in-design-lh}}}{1000 \times 3600} \rho_{\text{feed,plant}} C_{\text{p,feed}} (T_{\text{feed,in}} - T_{\text{HR,feed,out}})$$

$$(8.39) \quad P_{\text{thermal,cooler}} = \frac{M_{\text{perm,in-design-lh}}}{1000 \times 3600} \rho_{\text{water}} C_{\text{p,water}} (T_{\text{HR,perm,out}} - T_{\text{perm,in}})$$

$$(8.40) \quad P_{\text{thermal,HR}} = \frac{M_{\text{feed,in-design-lh}}}{1000 \times 3600} \rho_{\text{feed,plant}} C_{\text{p,feed}} (T_{\text{HR,feed,out}} - T_{\text{HR,feed,in}}) \\ = \frac{M_{\text{perm,in-design-lh}}}{1000 \times 3600} \rho_{\text{water}} C_{\text{p,water}} (T_{\text{HR,perm,in}} - T_{\text{HR,perm,out}})$$

where $P_{\text{electric,pumps}}$ is the electric consumption of the pumps in [W], $P_{\text{thermal,feed}}$, $P_{\text{thermal,heater}}$, $P_{\text{thermal,cooler}}$ and $P_{\text{thermal,HR}}$ are the thermal consumption of the heat exchanger to heat the feed from T_{intake} (taken equal to 20°C) and $T_{\text{feed,in}}$ and the ones of each intermediate heater, cooler and recovery heat

exchanger between MD modules [W]. $C_{p,feed}$ and $C_{p,water}$ are the specific heat of feed and water respectively in [kJ/(kg K)]. $T_{HR,feed,in}$, $T_{HR,feed,out}$, $T_{HR,perm,in}$ and $T_{HR,perm,out}$ are the inlet and the outlet temperatures of the feed and the permeate solutions in the recovery heat exchanger. Finally, ΔP_{in} is the inlet feed and permeate pressures [Pa], usually equal to 1.013E5 Pa.

8.4. MD Nomenclature

T	temperature [K]
m	volume flow rate [m ³ /s]
M	mass flow rate [kg/h]
C	concentration [ppm]
Q	heat flux [W/m ²]
h	heat transfer coefficient [W/(m ² K)]
Jw	water flux [kg/(m ² s)]
ΔH_{evap}	latent heat of vaporization of water [J/kg]
k_m	membrane thermal conductivity [W/(m K)]
k_{air}	air thermal conductivity [W/(m K)]
$k_{membr,pol}$	polymeric structure thermal conductivity [W/(m K)]
k	thermal conductivity of the solution [W/(m K)]
Nu	Nusselt number [-]
Re	Reynolds number [-]
Pr	Prandtl number [-]
Sh	Sherwood number [-]
Sc	Schmidt number [-]
D_h	hydraulic diameter of the channel [m]
v	fluid velocity in the channel [m/s]
C_p	fluid specific heat [J/(kg K)]
L	channel length [m]
B_m	mass transfer coefficient [kg / (m ² s Pa)]
ΔP_{in}	inlet pressure [Pa]
R	ideal gas constant (8.314 J/(K mol))
k_B	Boltzmann constant (1.38066×10^{-23} J/K)
d_{wat}	collision diameter of water vapor [m]
P_{pore}	pressure within the pores [Pa]
r_{pore}	pore radius [m]
P_{air}	air pressure inside the pores [Pa]
$D_{w,k}$	Knudsen diffusion coefficient [m ² /s]
$D_{w,m}$	molecular diffusion coefficient [m ² /s]
$D_{NaCl,wat}$	diffusivity of NaCl in water [m ² /s]
$k_{f, mass}$	mass transfer coefficient in the feed channel [m/s]
$N_{parallel}$	number of branches in parallel [-]
$N_{tot, modules}$	total number of modules present in the plant [-]
A_{module}	membrane area of a single module [m ²]
$P_{electric, pumps}$	electric consumption of the pumps [W]
$P_{thermal, feed}$	thermal consumption of the heat exchanger to heat the feed cooler [W]
$P_{thermal, heater}$	thermal consumption of the intermediate heater [W]
$P_{thermal, cooler}$	thermal consumption of the intermediate cooler [W]
$P_{thermal, HR}$	thermal consumption of the intermediate recovery heat exchanger [W]
Subscripts	
m	membrane

f	feed
p	permeate
m,hot	feed membrane interface
m,cold	permeate membrane interface
bulk,hot	feed bulk
bulk,cold	permeate bulk
conv,hot	convective flux, feed side
conv,cold	convective flux, permeate side
cond,m	conductive flux, membrane
evap,m	latent heat, membrane
in	inlet in the element
out	outlet of the element
feed,plant	solution fed to the plant
brine,plant	concentrate solution produced by the plant
dist,plant	distillate solution produced by the plant
perm,in-design-lh	design inlet permeate of the module (flow rate in [l/h])
feed,in-design-lh	design inlet feed of the module (flow rate in [l/h])

Greek letters

δ_m	membrane thickness [m]
ϵ	membrane porosity [-]
ρ	solution density [kg/m^3]
μ	dynamic viscosity of the fluid [$\text{kg}/(\text{m s})$]
λ	molecular mean free path [m]
τ	membrane tortuosity [-]

Acronyms

MD	membrane distillation
DCMD	direct contact membrane distillation
AGMD	air gap membrane distillation
SGMD	sweep gas membrane distillation
VMD	vacuum membrane distillation

9. Ion Exchange Resins Model

Ion Exchange resins (IEX) provide the interchange of ions between two phases, i.e. a resin phase and a liquid phase. The resin is a cross-linked polymer network, which presents a relatively uniform distribution of active sites, consisting in functional groups and ions, electrostatically bound (Alexandratos 2009). When the resin is surrounded by a solution containing ions of the same charge, an ion exchange occurs: the ions before dissolved in the solution get bound to the resin, while the ions before bound to the resin move to the liquid phase, as it is reported in Figure 14. The main advantage of the ion exchange resins technology consists in the reversibility of the ion exchange: there is no permanent change in the structure of the resin and it is possible to reuse the ion exchange material after having regenerated it (Wheaton and Lefevre 2016). Therefore, the technology provides the alternation of two phases: a loading phase, where the ions present in the feed solution are entrapped by the resin, and a regeneration phase, where a regenerant solution is employed to bring the resin back to the initial condition. In particular, during the regeneration phase,

the ions that were entrapped in the resin sites are substituted with corresponding ions, present in the regenerant solution and initially bound to the resin active sites (e.g. Na^+ in the case of Figure 14).

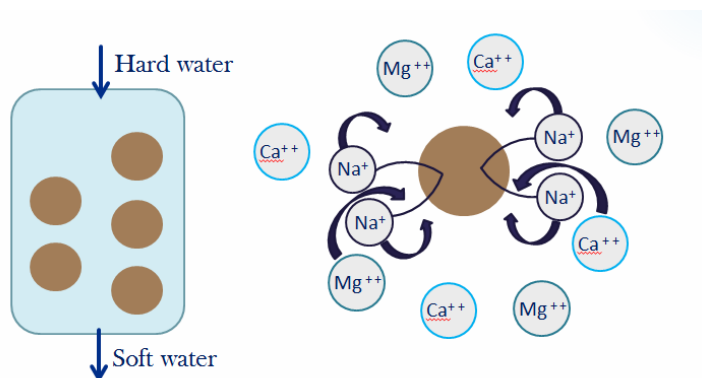
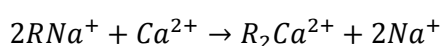


Figure 14: Schematic representation of the loading phase for IEX resins used for water softening

For example, in water softening, the reaction occurring in the loading phase is:



while the inverse reaction occurs during the regeneration phase. In the direct reaction, the exchanger R can exchange the bound ion Na^+ for the Ca^{2+} ions present in the hard water, so the calcium is removed from the water and the equivalent quantity of sodium is released to the solution. When all the active sites are occupied by Ca^{2+} or Mg^{2+} ions, the resin has to be regenerated through the employment of a regenerant solution of NaCl, in order to bring the sites back to the Na^+ form and the resin can be reused (Alexandratos 2009).

The IEX resins are employed for several applications, for example for softening/dealkalization, organic scavenging, demineralization, nitrate or boron removal and accordingly several different types are available in the industry. The resins are typically categorized into cation and anion exchange resins and within both categories a further sub-categorisation into strong and weak resins is performed in literature (Wheaton and Lefevre 2016). Within the cation exchange resins, the weak resins have a high affinity with hydrogen ions and are typically regenerated via the employment of strong acids, conversely the strong resins are able to exchange cations and to split neutral salts and are typically regenerated via a NaCl solution. Regarding the anion exchange resins, the weak resins are used for the sorption of strong acids and are regenerated via caustic soda, while the strong resins have greater affinity for weak acids, as the ones commonly present in the water to be demineralized. In the following, the model of IEX resins employed for water softening with co-current regeneration is described. The model structure then can be readapted, when necessary, to other applications, modifying the input feed composition, the resin properties and the regenerant solution.

9.1. Model for IEX Resins for Water Softening

The model follows the structure of the commercial software WAVE for IEX design and it is able to calculate the main outputs relevant to both the loading and the regenerant phase, e.g. the required

resin volume, the feed velocity in crossing the resin bed, the required regeneration time and volume. All the inputs and outputs of the model are listed in Table 12.

Table 12: Inputs and Outputs of the IEX model

Inputs	Outputs
Feed flow rate [m ³ /h]	Resin volume [m ³]
Feed composition [ppm]	Ionic load [eq]
Feed hardness [eq/L]	Linear [m/h] and specific [BV/h] feed velocity
Train configuration	Resin area [m ²] and bed depth [m]
Duration of the operating cycle [h]	Regeneration ratio [%]
Resin and regeneration type	Applied and excess regenerant per cycle [eq]
Regenerant concentration [%wt]	Gross and net throughput [m ³]
Regeneration temperature [°C]	Total regeneration volume [m ³]
Regeneration dose [g/L _{resin}]	Total regeneration time [h]
Regeneration condition (backwash duration and expansion, injection velocity, rinse volume)	Duration and volume of the regeneration phases (backwash, injection, displacement and fast rinse)
Max pressure drop in the resin bed [bar]	IEX recovery [%]
Max hardness in the effluent [ppm CaCO ₃]	Hardness leakage [ppm CaCO ₃]

The model presents an iterative procedure, where the value of the required resin volume calculated in the previous iteration is given as the starting value for the calculation of the other variables in the following iteration. The iterative procedure stops as soon as the difference between the guess and the calculated volume is lower than a certain tolerance (i.e. 1e-4). The procedure starts with the feed and the resin characterization. For what concerns the feed, the concentration of every ion is converted into [eq/L] and the TDS of the feed is estimated in [eq/L] and in [ppm CaCO₃]. For what concerns the resin characterization, once a resin type is defined, the operating capacity can be calculated, on the basis of the information reported in the resin data sheet (*DOWEX Marathon C Resin - Product Data Sheet* n.d.). For example, for Dowex Marathon C resin in the Na form, the operating capacity can be calculated as function of the regeneration dose, according to Figure 15. For the effective operating capacity, a safety factor is used and its value is taken equal to 0.95, as in the Wave software.

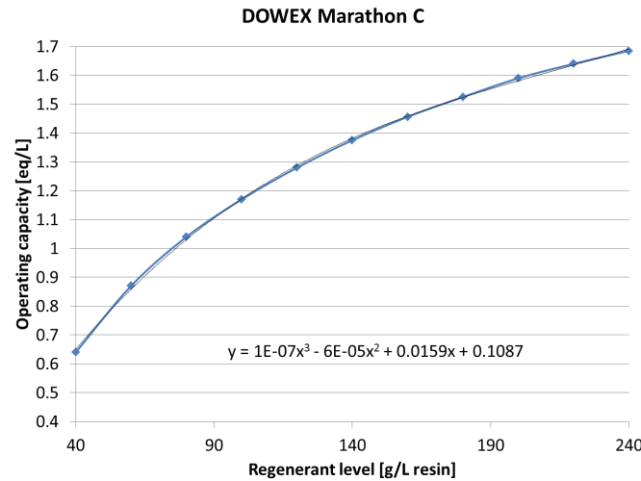


Figure 15: Operating capacity of DOWEX Marathon C resins for water softening

At this point, the solving procedure starts with a guess resin volume V_{resin} and cross section area A_{resin} . The feed flow rate (Q_{feed} [m^3/h]) to be considered in the procedure depends on the train configuration, since, often, two or more trains online and one train for the regeneration are accounted. Thus, the total feed flow rate has to be divided by the number of trains online. Moreover, the feed water is also used for one of the regeneration stages, the fast rinse, which is the final part of the regeneration, used to flush out the excess regenerant (*DOWEX Ion Exchange Resins Water Conditioning Manual* n.d.). For this reason, the net feed water processed in a cycle depends on the total feed water fed to the train and on the amount required by the fast rinse. Consequently, the gross throughput, defined as the total amount of water which is processed during the service cycle in m^3 , is calculated as follows:

$$(9.1) \quad \text{throughput}_{\text{gross}} = Q_{\text{feed}} t_{\text{cycle}} - V_{\text{fast rinse}}$$

where t_{cycle} is the duration of the operating cycle in hours and $V_{\text{fast rinse}}$ is the total volume required by the last regeneration stage in m^3 . Thus, the net feed water flow rate ($Q_{\text{feed,net}}$) is given by the ratio between the $\text{throughput}_{\text{gross}}$ and t_{cycle} . At this point, the feed linear velocity in m/h and the feed specific velocity in BV/h (bed volumes per hour) can be calculated as $Q_{\text{feed,net}} / A_{\text{resin}}$ and $Q_{\text{feed,net}} / V_{\text{resin}}$ respectively. The ionic load is defined as the total amount of equivalents that can be exchanged by the resin bed, thus it can be calculated as:

$$(9.2) \quad \text{Ionic load} = C_{\text{eff,op}} V_{\text{resin}} 1000$$

where $C_{\text{eff,op}}$ is the effective operating capacity in $[\text{eq}/\text{L}]$.

The net throughput is defined as the amount of water produced in the operating cycle and it takes into account the fact that part of the water produced is used for the other regeneration stages, i.e. the backwash, injection and displacement (or slow) rinse.

$$(9.3) \quad \text{throughput}_{\text{net}} = \text{throughput}_{\text{gross}} - V_{\text{backwash}} - V_{\text{injection}} - V_{\text{displ rinse}}$$

In analogy with the net feed water flow rate, the net product flow rate ($Q_{\text{prod,net}}$) is calculated as the ratio between throughput_{net} and t_{cycle} . Finally, the IEX recovery is defined as the ratio between the throughput_{net} and the total amount of water supplied during the operating cycle per train. For the first guess, $Q_{\text{feed,net}}$ and $Q_{\text{prod,net}}$ are assumed to be equal to Q_{feed} , so the IEX recovery is assumed to be 100%.

For what concerns the regeneration phase, the regeneration dose R_{dose} , i.e. the amount of regenerant used per cycle in [g/L_{resin}], is given as an input, together with the concentration of the regenerant solution R_{conc} . From the regeneration dose, it is possible to define the regeneration ratio R_{ratio} , i.e. the reciprocal of the regeneration efficiency, being it defined as the ratio between the total applied regenerant and the ionic load.

$$(9.4) \quad R_{\text{ratio}} = \frac{R_{\text{dose}}/MW_{\text{NaCl}} V_{\text{resin}} 1000}{C_{\text{eff,op}} V_{\text{resin}} 1000} \times 100$$

$$(9.5) \quad \text{Applied regenerant} = R_{\text{dose}}/MW_{\text{NaCl}} V_{\text{resin}} 1000$$

$$(9.6) \quad \text{Excess regenerant} = \text{Applied regenerant} - \text{Ionic load}$$

Moreover, the duration of the regeneration cycle can be evaluated by investigated all the single regeneration phases. The backwashing is performed before the injection of the regenerant solution and it consists of an upward flow to remove all the materials covering the resin. The duration is usually fixed (e.g. 15 min) together with the bed expansion occurring during the backwashing. If the bed expansion is given, a linear correlation between expansion and water flow rate, usually supplied by the resin manufacturer in the data sheet, is applied to calculate the water flow rate (*DOWEX Ion Exchange Resins Water Conditioning Manual* n.d.). Regarding the injection phase, the flow rate is usually given as a parameter (e.g. specific flow rate equal to 3.5 BV/h). The required injection time is calculated taking into account the total amount of regenerant that has to be supplied (applied regenerant [eq]) and the concentration of the solution, according to the following expression:

$$(9.7) \quad t_{\text{injection}} = \frac{\text{Applied regenerant}}{\frac{R_{\text{conc}}}{MW_{\text{NaCl}}} Q_{\text{injection}}}$$

where R_{conc} is the concentration of the regenerant solution [ppm] and $Q_{\text{injection}}$ is the injection flow rate in m³/h. Finally, the last stages of the regeneration cycle provide a rinse, i.e. the passage of water through the resin bed to flush out the remaining regenerant solution. Just after the injection, a displacement (slow) rinse is performed with the treated water and usually with the same flow rate as the regenerant in the injection phase. The total volume of water is usually given (e.g. 2 BV) and then the required time can be calculated. The second rinse step is faster and it usually operates at the same flow rate of the feed ($Q_{\text{feed,net}}$) and, also in this case, the volume is given as input (e.g. 3 BV) and the time is calculated.

Overall, the regeneration time ($t_{\text{regeneration}}$) is given by the sum of the backwash (t_{backwash}), injection ($t_{\text{injection}}$), displacement rinse ($t_{\text{displ rinse}}$) and fast rinse time ($t_{\text{fast rinse}}$) and the total regeneration volume

($V_{\text{regeneration}}$) is given by the sum of the volumes required by each of these stages. Once these volumes are calculated, they will be used as the guess values in the following iteration for the calculation of $\text{throughput}_{\text{gross}}$, $\text{throughput}_{\text{net}}$, $Q_{\text{feed,net}}$ and $Q_{\text{prod,net}}$.

At this point, the resin volume V_{resin} is recalculated according to the expression:

$$(9.8) \quad V_{\text{resin}} = \frac{\text{throughput}_{\text{gross}} \text{ hardness}_{\text{in}}}{C_{\text{eff,op}} 1000}$$

where $\text{hardness}_{\text{in}}$ is the inlet amount of Mg^{++} and Ca^{++} in meq/L. The resin cross-section area and the bed depth are calculated by imposing a maximum pressure drop across the resin bed. Therefore, the resin data sheet provides the trend of the pressure drop in [bar/m] vs. the flow rate, as shown for the DOWEX Marathon C resins in Figure 16 (*DOWEX Marathon C Resin - Product Data Sheet* n.d.). The shown pressure drops are measured at $T = 20^{\circ}\text{C}$. In order to calculate the pressure drops at a different temperature T [$^{\circ}\text{C}$], the following correlation is proposed for these specific resins:

$$(9.9) \quad P_T = \frac{P_{20^{\circ}\text{C}}}{0.026 T + 0.48}$$

Employing the pressure drop trend with the feed velocity (Figure 16) and the correction with the temperature (usually the temperature used for the estimation of pressure drops is 0°C), it is possible to calculate the cross section area and the height of the resin bed in correspondence to a total pressure drop of 1bar.

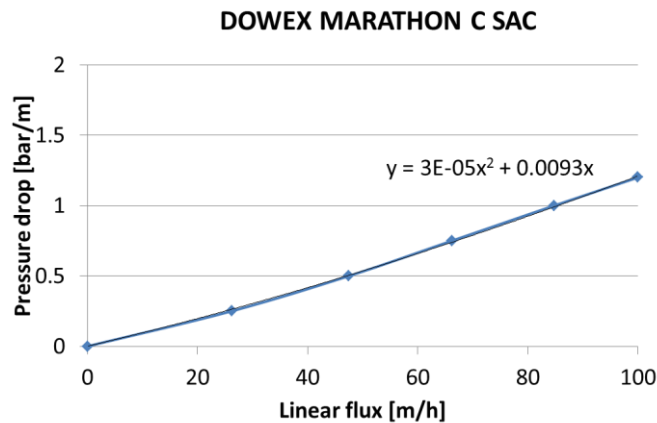


Figure 16: Trend of the pressure drop [bar/m] with the linear flux [m/h] for the DOWEX Marathon C Strong Acid Cation resins

The values of resin volume, area and bed depth are then updated in the following iteration and all the calculations are repeated, until the whole system results to be solved.

Finally, it is possible to calculate the system leakage, which corresponds to the hardness still present in the treated water. The leakage [ppm CaCO_3] is function of the feed TDS in ppm CaCO_3 according to a linear correlation of the generic form:

$$(9.10) \quad \text{leakage} = A TDS_{feed} - B$$

where A and B depend on the regeneration dose. Different linear trends of leakage vs. TDS_{feed} were reported in the resin data sheet at different regeneration dose, for this reason more general correlations for A and B in function of the regeneration dose were derived, as shown in Figure 17. If the leakage is higher than the maximum value given as input, the regeneration dose should be increased and the calculation performed again.

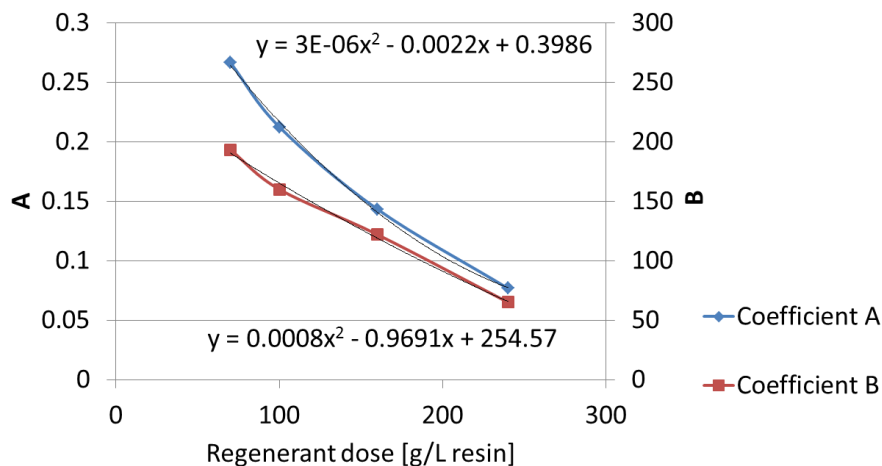


Figure 17: Trends of the coefficients A and B used in Equation 9.10 as function of the regenerant dose

9.2. IEX Nomenclature

V_{resin}	required volume of the resins [m^3]
A_{resin}	section of the resins [m^2]
Q_{feed}	feed flow rate [m^3/h]
t_{cycle}	duration of the operating cycle[h]
MW_{NaCl}	molecular weight of NaCl [mol/g]
$V_{backwash}$	total regenerant volume required by the backwash stage during regeneration [m^3]
$V_{injection}$	total regenerant volume required by the injection stage during regeneration [m^3]
$V_{displ\ rinse}$	total regenerant volume required by the displacement rinse during regeneration [m^3]
$V_{fast\ rinse}$	total regenerant volume required by the fast rinse during regeneration [m^3]
$V_{regeneration}$	total regenerant volume required [m^3]
$t_{backwash}$	backwash time during regeneration [h]
$t_{injection}$	injection time during regeneration [h]
$t_{displ\ rinse}$	displacement rinse time during regeneration [h]
$t_{fast\ rinse}$	fast rinse time during regeneration [h]
$t_{regeneration}$	regeneration time [h]
$Q_{feed,net}$	net feed flow rate [m^3/h]
$C_{eff,op}$	effective operating capacity [eq/L]
$Q_{prod,net}$	net product flow rate [m^3/h]
R_{dose}	regeneration dose [g/L _{resin}]
R_{ratio}	regeneration ratio [%]
R_{conc}	concentration of the regenerant solution [ppm]
T	operating temperature [$^{\circ}C$]

P_T	pressure drop at T [bar/m]
TDS_{feed}	concentration of the feed [ppm $CaCO_3$]
A	constant for the calculation of the leakage
B	constant for the calculation of the leakage
hardness _i	inlet amount of Mg^{++} and Ca^{++} [meq/L]

Acronyms

IEX	Ion Exchange
-----	--------------

10. Eutectic Freeze Crystallization Model

10.1. Data driven numerical Model

Based on Hassan et al. provided data an statistic approach of the EFC modeling has been done. The problem with this statistical model is that it only allows interpolation, not extrapolation, since it uses Dealunay patterns. When the requested information is out of range it issues an error. As the data on which the model is based are those of the Hassan et al article (Hassan et al, 2017), its minimum and maximum values are those that hold the range of operation of the model. The model consists of 3 files:

a) *efcStatSingle.m*: This is to calculate a given scaling induction time value. The file must edit the values of N and DT, which are the rotation speed in rpm and the difference of sub-cooling temperatures in C, respectively. There are comments on the file indicating it. Returns the induction time in seconds.

b) *efcStatSweepPlot.m*: This allows you to sweep through different temperature differentials at a specific rotation speed. DT0 is the value of the temperature difference from which the sweep begins, and it is the number of increments (tenths of a degree). Returns a graph of induction time vs. temperature differential for a specific rotation speed.

c) *efcStatSweepFile.m*: does the same as the previous one but instead the output is a graph is a data file in two columns (temperature-time difference).

10.2. Thermodynamic EFC Model

Eutectic freezing crystallization operates at the eutectic temperature/point of a binary solution. In this method, salts separate as solids and fresh water separates as ice from brine simultaneously. Both salt and ice nucleates and grow independently. This gives the advantage of easy separation process since ice floats and the salt sinks by density difference. Though, very low operating temperature (-20 to -25 °C) and thus additional cost of eutectic freezing is required compared to other freezing methods. Following any of the mentioned methods separation and melting comes at the end. The formed ice block is collected in the ice crystal separator where they are washed with water to purify blocks' surfaces and recover the solutes involved. However, the main disadvantages of freeze crystallization process compared with evaporation and RO is the incurred operational costs during the ice separation process (Kucera 2014). Separation is usually done by washing the surface of the produced ice blocks with pure fresh water. Melting of pure ice blocks finally takes place either

directly or indirectly contact. However, energy recovery is one of the important aspects of this process and needs to be taken in highly consideration.

Thus, besides the statistical model, a first thermodynamic version of the model is an attempt to obtain a mathematical expression for the ice scaling thickness and its purity as a function of the variables of interest: time, temperature, concentration and rotational speed. However, the current version of the model does not take rotation into account, as the first experimental tests will be run in a static medium. The effect of the rotational speed will be implemented in the model in the next version.

Once the ice scaling thickness is determined, the overall heat transfer can be evaluated. The model is formulated under the following hypothesis:

- Eutectic freeze crystallization: both ice and salt crystallize simultaneously and grow at the same rate.
- Perfect mixing: temperature and concentration are uniform everywhere within the vessel.
- There are no heat losses in the whole system.
- The thickness of the ice scaling is much smaller than the vessel radius.
- Crystals are considered to be spherical in shape.
- The temperature at the inner side of the ice scaling is equal to the slurry temperature.

The nucleation rate, in number of crystals formed by volume and time units, can be expressed as:

$$(10.1) \quad B = b_1 \exp\left(\frac{-b_2}{T}\right)$$

where b_1 and b_2 are constants to be determined and T is temperature. The effective nucleation rate, in number of crystals by time unit, is:

$$(10.2) \quad B_{eff} = B(1 - \Phi)V$$

where Φ is the volume fraction of crystals, both ice and salt, inside the vessel and V the total volume of the vessel without internal elements.

The growth rate of the crystals, even if there are different opinions among authors and there seems not to be a clear established criterion, can be approximated as:

$$(10.3) \quad G = g_1 \exp\left(\frac{-g_2}{T}\right) (C - C_{eq})$$

where g_1 and g_2 are constants to be determined, C is the concentration of the substance crystallizing in the solution and C_{eq} the equilibrium concentration.

The total volume of crystals in each time step is:

$$(10.4) \quad v_{cT}^i = \sum N_c^i v_c^j$$

where N_c is the number of crystals formed at time step i and v_c the volume of crystal formed at time step j . Subscripts i and j vary to take into account that the first crystals formed will be the largest ones. The number of crystals formed at each time step is:

$$(10.5) \quad N_c^i = B_{eff}^i \Delta t$$

where Δt is the time step, which is considered uniform. The crystal volume is determined by:

$$(10.6) \quad v_c = \frac{4}{3}\pi(r^{i-1} + G^i \Delta t)^3$$

Where r is the radius of the crystal. The volume fraction of crystals inside the vessel is, then:

$$(10.7) \quad \phi = \frac{v_{cT}}{V}$$

Since the interest lies in obtaining a correlation from experimental data via coefficient adjustment, then we can assume, recalling Eq. 10.5, that the total number of crystals formed is

$$(10.8) \quad N_c \sim B_{eff} t = B(1 - \phi)Vt$$

Therefore

$$(10.9) \quad N_c = b_1 \exp\left(\frac{-b_2}{T}\right) (1 - \phi)Vt$$

Combining the expressions for the crystal volume (10.6) and growth rate (10.3) presented earlier, the crystal volume can be obtained as

$$(10.10) \quad v_c = \frac{4}{3}\pi \left(r_0 + g_1 \exp\left(\frac{-g_2}{T}\right) (C - C_{eq})t \right)^3$$

So, the total volume of crystals can be approximated as

$$(10.11) \quad v_{cT} = b_1 \exp\left(\frac{-b_2}{T}\right) (1 - \phi)Vt \frac{4}{3}\pi \left(r_0 + g_1 \exp\left(\frac{-g_2}{T}\right) (C - C_{eq})t \right)^3$$

Since the total volume of crystals is related to the total volume of the vessel by the crystal volume fraction (Eq. 10.7), then

$$(10.12) \quad \phi V = b_1 \exp\left(\frac{-b_2}{T}\right) (1 - \phi)Vt \frac{4}{3}\pi \left(r_0 + g_1 \exp\left(\frac{-g_2}{T}\right) (C - C_{eq})t \right)^3$$

This model can be simplified by neglecting the initial radius of the crystal ($r_0=0$), which seems reasonable specially at long times. In order to facilitate reading, some constant parameters can be grouped:

$$(10.13) \quad \alpha_1 = b_1 \frac{4}{3} \pi g_1^3$$

So

$$(10.14) \quad \phi = \alpha_1(1 - \phi) \exp\left(\frac{-b_2}{T}\right) \left(\exp\left(\frac{-g_2}{T}\right)\right)^3 (C - C_{eq})^3 t^4$$

After some mathematical manipulation, the following expression for the crystal volume fraction can be obtained

$$(10.15) \quad \phi = \alpha_1(1 - \phi)(C - C_{eq})^3 t^4 \exp\left(\frac{-b_2 - 3g_2}{T}\right)$$

Regrouping some more parameters:

$$(10.16) \quad \alpha_2 = -b_2 - 3g_2$$

and then

$$(10.17) \quad \phi = \alpha_1(1 - \phi)(C - C_{eq})^3 t^4 \exp\left(\frac{\alpha_2}{T}\right)$$

After some more mathematical manipulation:

$$(10.18) \quad \phi = \frac{\alpha_1(C - C_{eq})^3 t^4 \exp\left(\frac{\alpha_2}{T}\right)}{1 + \alpha_1(C - C_{eq})^3 t^4 \exp\left(\frac{\alpha_2}{T}\right)}$$

$$(10.19) \quad \frac{1}{\phi} = \frac{1}{\alpha_1(C - C_{eq})^3 t^4 \exp\left(\frac{\alpha_2}{T}\right)} + 1$$

A volume fraction of scaling is defined as ϕ_s , with the volume of scaling being

$$(10.20) \quad V_s = \phi_s V$$

This volume of scaling can be also expressed in terms of the vessel geometry:

$$(10.21) \quad V_s = \pi R_i^2 L - \pi(R_i - \gamma)^2 L$$

where γ is the scaling thickness. Considering the scaling thickness much smaller than the vessel radius, then after some mathematical manipulation the volume of scaling can be defined as

$$(10.22) \quad V_s \approx 2\pi R_i \gamma L$$

Another parameter which will be useful is now defined:

$$(10.23) \quad \alpha_3 = \frac{V_s}{v_{cT}}$$

Substituting into the previously derived equation for the crystal volume fraction (10.19):

$$(10.24) \quad \frac{V}{v_{cT}} = \frac{1}{\alpha_1(C - C_{eq})^3 t^4 \exp\left(\frac{\alpha_2}{T}\right)} + 1$$

$$(10.25) \quad \frac{\alpha_3 V}{V_s} = \frac{1}{\alpha_1(C - C_{eq})^3 t^4 \exp\left(\frac{\alpha_2}{T}\right)} + 1$$

Introducing the expression for the volume of scaling (10.22):

$$(10.26) \quad \frac{\alpha_3 V}{2\pi R_i \gamma L} = \frac{1}{\alpha_1(C - C_{eq})^3 t^4 \exp\left(\frac{\alpha_2}{T}\right)} + 1$$

and after some more mathematical manipulation:

$$(10.27) \quad \gamma = \frac{\alpha_3 V \alpha_1 (C - C_{eq})^3 t^4 \exp\left(\frac{\alpha_2}{T}\right)}{2\pi R_i L \left(\alpha_1 (C - C_{eq})^3 t^4 \exp\left(\frac{\alpha_2}{T}\right) + 1 \right)}$$

Another parameter grouping variables is defined for the sake of clarity:

$$(10.28) \quad \alpha_4 = \frac{2\pi R_i L}{V}$$

Substituting, manipulating and rearranging an expression for the scaling thickness is obtained:

$$(10.29) \quad \gamma = \frac{\alpha_1 \alpha_3 (C - C_{eq})^3 t^4 \exp\left(\frac{\alpha_2}{T}\right)}{\alpha_4 \left(\alpha_1 (C - C_{eq})^3 t^4 \exp\left(\frac{\alpha_2}{T}\right) + 1 \right)}$$

Since α_4 is a geometrical parameter, the previous expression becomes:

$$(10.30) \quad \gamma = \frac{V}{2\pi R_i L} \frac{\alpha_1 \alpha_3 (C - C_{eq})^3 t^4 \exp\left(\frac{\alpha_2}{T}\right)}{\left(\alpha_1 (C - C_{eq})^3 t^4 \exp\left(\frac{\alpha_2}{T}\right) + 1 \right)}$$

where α_1 , α_2 and α_3 are parameters to be determined experimentally.

As for the purity of the crystals, the impurity concentration within the crystal can be calculated through:

$$(10.31) \quad C_{ic} = k_{diff} C_{il} \frac{\rho_c}{\rho_l}$$

where C_{il} is the impurity concentration within the solution and ρ_c and ρ_l are the densities for the crystal and the liquid, respectively. k_{diff} is computed in the following manner:

$$(10.32) \quad k_{diff} = f \left\{ \frac{C_{il}}{\rho_l - C_{il}} \left[\exp\left(\frac{G\rho_c}{k_d \rho_l}\right) - 1 \right] \right\}$$

where f expresses that k_{diff} is a function of what is inside (in a first approach it can be considered a linear function and thus f is another parameter to be determined) and k_d is the mass transfer coefficient.

In order to link the ice scaling with the total heat transfer, the model can be completed assuming that there are no heat losses. Therefore, the total heat transfer can be defined as:

$$(10.33) \quad Q = \dot{m}_c C p_c (T_{c,out} - T_{c,in})$$

where m_c is the mass flow rate of the coolant, Cp_c is its specific heat and $T_{c,out}$ and $T_{c,in}$ are the temperatures of the coolant at the exit and inlet, respectively. This heat transfer can be also related to the crystallization within the vessel as:

$$(10.34) \quad Q = \dot{m}_f \Delta H_f$$

where the subscript f corresponds to the crystallized liquid and ΔH is the heat of crystallization.

Since one of the hypothesis of the model is that there are not heat losses, then:

$$(10.35) \quad Q = q_c = q_w = q_s = q_l$$

where the subscripts refer to the coolant (c), vessel wall (w), ice scaling (s) and slurry (l).

The heat transfer in each of those elements of the system is described by the following equations:

$$(10.36) \quad q_c = h_c 2\pi R_o L (T_o - T_c)$$

$$(10.37) \quad q_w = k_w 2\pi L \frac{(T_i - T_o)}{\ln\left(\frac{R_o}{R_i}\right)}$$

$$(10.38) \quad q_w = k_{ice} 2\pi L \frac{(T_{s,i} - T_i)}{\ln\left(\frac{R_i}{R_i - \gamma}\right)}$$

$$(10.39) \quad q_l = h_l 2\pi (R_i - \gamma) L (T_l - T_{s,i})$$

where h and k are the conductive and convective heat transfer coefficients, respectively, and the combined subscript s,i refers to the inner surface of the ice scaling. The overall heat transfer resistance, referred to the external area, can be computed as:

$$(10.40) \quad \frac{1}{U} = \frac{Q}{2\pi L R_o} \Delta T$$

$$(10.41) \quad \frac{1}{U} = \frac{1}{h_c} + \frac{R_o \ln\left(\frac{R_o}{R_i}\right)}{k_w} + \frac{R_o \ln\left(\frac{R_i}{R_i - \gamma}\right)}{k_{ice}} + \frac{R_o}{(R_i - \gamma) h_l}$$

Combining the previous set of equations for q , if the temperature of the inner surface of the scaling is equal to the temperature of the slurry, then after some mathematical manipulation the scaling thickness can be computed as:

$$(10.42) \quad \gamma = R_i - \frac{QR_i}{(T_l - T_i)2\pi Lk_{ice}}$$

and consequently, if the scaling thickness and slurry temperature are known, the total heat required can be estimated as:

$$(10.43) \quad Q = \left(1 - \frac{\gamma}{R_i}\right) (T_l - T_i) 2\pi Lk_{ice}$$

In the same manner, if the scaling thickness and total heat transfer are known, the slurry temperature can be estimated:

$$(10.44) \quad T_l = T_i + \frac{QR_i}{(R_i - \gamma)2\pi Lk_{ice}}$$

However, it must be checked if the hypothesis $T_{s,i}=T_l$ holds true in the experiments.

10.3. Experimental Validation

10.3.1. Objective

The experiments will serve to determine the following:

- Growth rate of the ice scaling
- Purity of the ice scaling
- Quantity and purity of both salt and ice crystals in the slurry
- Variation of the effective viscosity as a result of crystallization

The variables that affect the parameters to be studied are:

- Subcooling temperature
- Rotational speed
- Initial concentration
- Time

10.3.2. Experimental Campaign

The numerical model of the Eutectic Freeze Crystallization (EFC) allows determining the scaling induction time in the stirred crystallizer as a function of different variables, such as the temperature difference between the stirred tank wall and the bulk solution, the rotational speed in the crystallizer and the salt concentration, and under certain restrictions (ice purity). That scaling induction time, alongside some other variables, will allow computing the different overall output parameters of interest. Nevertheless, numerical simulation must be validated. This task is being planned to be

carried out in the next few months at CTM once a new 5 litres EFC reactor will be fully implemented in a test-rig in the last trimester of 2018.

A synthetic 4 wt% Na₂SO₄ (aq) solution will be prepared by dissolving analytical-grade Na₂SO₄ from Merck (>99%) in deionized water of resistivity 6.2 MΩcm. Dissolution will be performed at room temperature under 300 rpm mixing condition for 30, 60, 90 and 120 min. Experiments will be conducted at different temperature driving forces DTML (bulk, secondary flow) and the rotational speed of the impeller (e.g., 100 rpm, 200 rpm, 300 rpm), at a constant level of initial undercooling of about 0.25 C and residence time described previously in an experimental setup.

The experiments will be conducted in a 5-L jacketed vessel type crystallizer (supplied by VidraFoc, Barcelona, Spain) with a concave bottom section to facilitate the settling of salt crystals. The ice slurry is expected to overflow through the top section. The crystallizer is insulated properly to prevent heat loss to the environment. A paddle with two blades is located in the middle section of the crystallizer and connected to a motor to agitate the solution in the crystallizer.

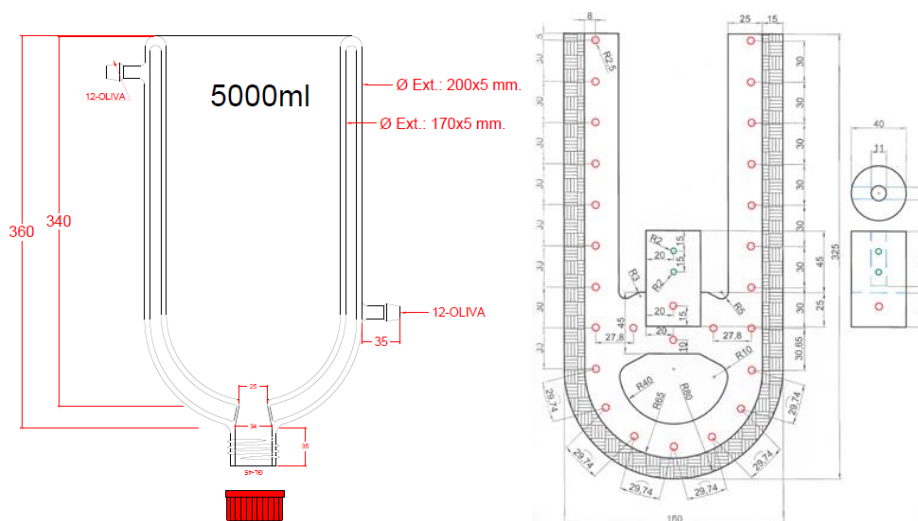


Figure 18: EFC Reactor layout

The feed solution will be pre-cooled by a heat exchanger in which the thermal fluid coolant is pumped by a cryo-compact Julabo Thermal Bath CF31 (supplied by Julabo, Seelbach, Germany). The temperature of the crystallizer content is controlled indirectly by means of a silicone oil coolant flowing through the crystallizer jacket. The coolant is circulated through the jacket of the crystallizer and exchanged heat with the solution inside the crystallizer. A DIN 1/10 PT100 temperature sensor with an accuracy of ± 0.01 °C will be used to measure the temperature of the solution. The onset of ice-scaling in the middle part of the crystallizer wall will be detected by visual inspection focused on the crystallizer wall adjacent to the coolant inlet in the jacket, which is likely to form ice scale first in the crystallizer. A light source will also be used to illuminate that part of the crystallizer. Compressed air is expected to be used to blow deposited condensate on the focused area in order to get a clear image.

Determining the induction time for ice-scaling (tind) is a method that can be used to control and extend the requirements of EFC processes. In this work, tind has been defined as the time elapsed after adding seed-ice to the solution to the onset of ice-scaling on the crystallizer wall.

The physical properties of the 4 wt% Na₂SO₄ (aq) solution will be obtained by using the correlation (Hasan and Louhti-Kultanen 2015) (Hasan et al. 2017).

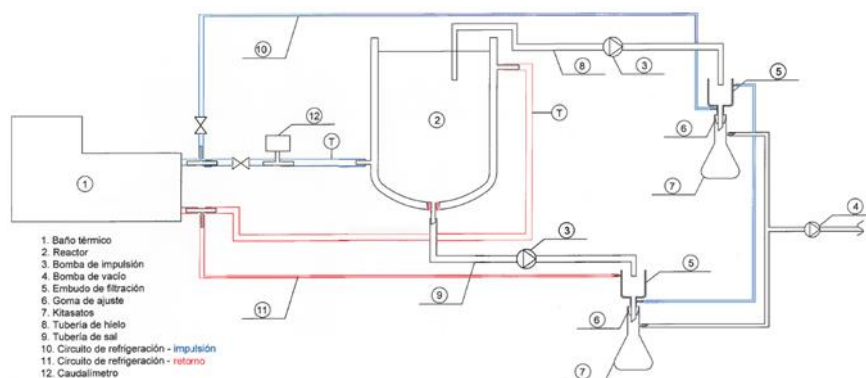


Figure 19: EFC Reactor experimental diagram

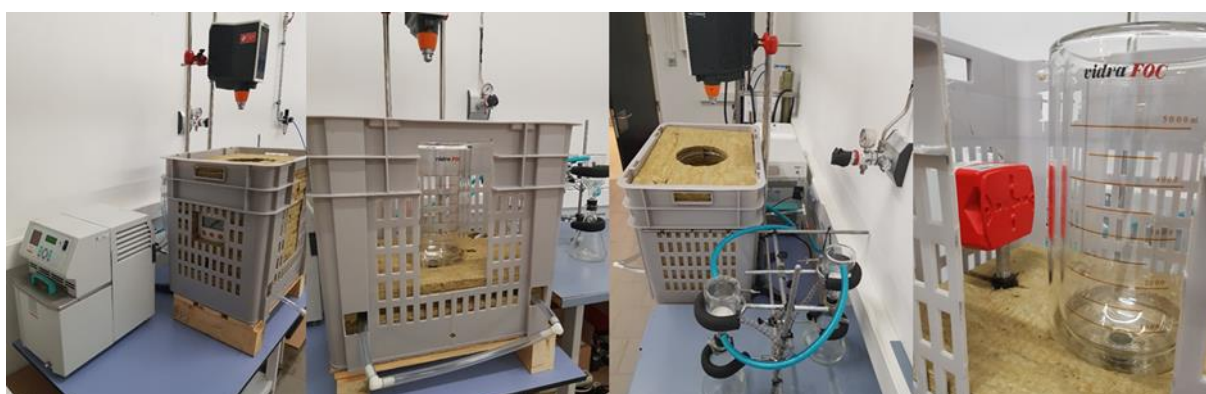


Figure 20: EFC Reactor layout

In order to complete a successful experimental campaign, it is critical to obtain separately the four phases present in the vessel: ice scaling, liquid and both salt and ice crystals at the bulk. A sufficient number of experiments should be carried out to properly determine the influence of each of the variables. However, due to the large number of experiments required, there will be two experimental campaigns. The first one will serve to determine the influence of time, subcooling temperature and rotational speed, while the second one will yield the influence of the initial concentration and the effect of the variation of viscosity. Table 11 summarizes the experiments to be carried out during the first campaign with a fixed initial concentration.

Table 11. Experiments planned for the first experimental campaign

Experiment	Subcooling (K)	Rotational speed (rpm)	Time (min)
1	0.25	0	30
2	0.25	0	60

3	0.25	0	90
4	0.25	0	120
5	1.00	0	30
6	1.00	0	60
7	1.00	0	90
8	1.00	0	120
9	4.00	0	30
10	4.00	0	60
11	4.00	0	90
12	4.00	0	120
13	0.25	300	30
14	0.25	300	60
15	0.25	300	90
16	0.25	300	120
17	1.00	300	30
18	1.00	300	60
19	1.00	300	90
20	1.00	300	120
21	4.00	300	30
22	4.00	300	60
23	4.00	300	90
24	4.00	300	120

The quantity of each of the phases will be measured by voiding the vessel, filtering the bulk and separating the salt and ice crystals. Then, the ice scaling will melt. At the end, the four different phases will be obtained separately and weighted. To obtain the concentration of each phase an electrical conductivity sensor will be used. Finally, the ice scaling thickness will be measured through a semi-numerical approach, considering the geometry of the ice, which depends on the temperature difference.

As commented previously, the goal of a combined EFC-Waste Heat Recovery System will be the maximization of COP_{th}, COP_{el} of the system (waste heat is used to drive a chiller in order to deliver cooling), control of ice growth velocity (function of the other conditions, such as temperature and concentration differences) and ice purity. Ice growth velocity is directly related to ice purity. These data will be used as the basis to define different control strategies of cooling delivery in order to evaluate waste heat recovery potential, being directly transformed to energy savings.

11. Process Models and Simulation Tools for Electrodialysis

In order accurately to describe the electrodialysis (ED) process and develop effective process simulation tools it is necessary to implement mathematical models able to take into account a number of complex phenomena. These include:

- Solution-membrane equilibria;
- Concentration polarization;
- Fluid flow behavior along channels;
- Mass transport phenomena;
- Mass balance in the compartments;
- Electrical phenomena and etc.

Several different modeling approaches have been presented so far in the literature, each one addressing in a different way and to a different extent all these aspects. These modeling tools are generally classified into **simplified** and **advanced** modeling approaches.

The first class of process models is characterized by a highly simplified approach based on neglecting most non-ideal phenomena (e.g. diffusion boundary layer, non-Ohmic effects, salt diffusion, water fluxes, etc.) and on the use of lumped parameters equation (i.e. the use of average compartment concentrations to estimate all process variables). Simplified models are commonly adopted for a first rough design of ED equipment, allowing the estimation of figures such as the membrane area required for a given separation problem, and for simplified economic analysis of the process. In this case, empirical coefficients are applied in order to somehow account for all non-idealities, often summarized by a simple current utilization factor (or current efficiency).

The second, and wider, class of process models can be divided into 2 sub-categories: 1) rigorous Nernst-Planck (N-P) or Stefan-Maxwell (S-M) based *theoretical models* and 2) *semi-empirical models*. In both cases, non-ideal phenomena are accounted for and models typically include mass balance differential equations in order to describe the variation of process parameters along the flow direction. The main difference between the two sub-categories is related to the mathematical description of trans-membrane phenomena.

N-P based models (S-M models are even more complex and accurate, with this respect) contain rigorous equations able to almost predictively describe all transport phenomena inside the membrane at the microscopic level (though even in this case some membrane features, such as ions diffusivity, ions mobility, fixed charge density etc. have to be based on empirical information). The simulation is often carried out using Finite Element Methods (or similar approaches) and the process model is practically merged with thermodynamics and mass transfer models, including the description of the fluid dynamics. A limitation of this approach is the very large computational power required to solve the model, which limits the application to very simple channel geometries or to a very small computational domain, thus making the tool unsuitable for whole-stack simulation purpose.

Semi-empirical models, on the contrary, are based on a multi-scale approach, in which lower scale phenomena (such as mass transfer and fluid behavior, leading also to the characterization of diffusion boundary layer) are described by means of empirical information or small-scale theoretical analysis, e.g. by means of Computational Fluid Dynamics tool. Thus, also effect of spare geometry or membrane profiles can be accounted for. Meso-and higher-scale phenomena are described by

means of differential equations for mass balances and algebraic phenomenological equations for fluxes through the membrane, allowing for the achievement of plant-scale description.

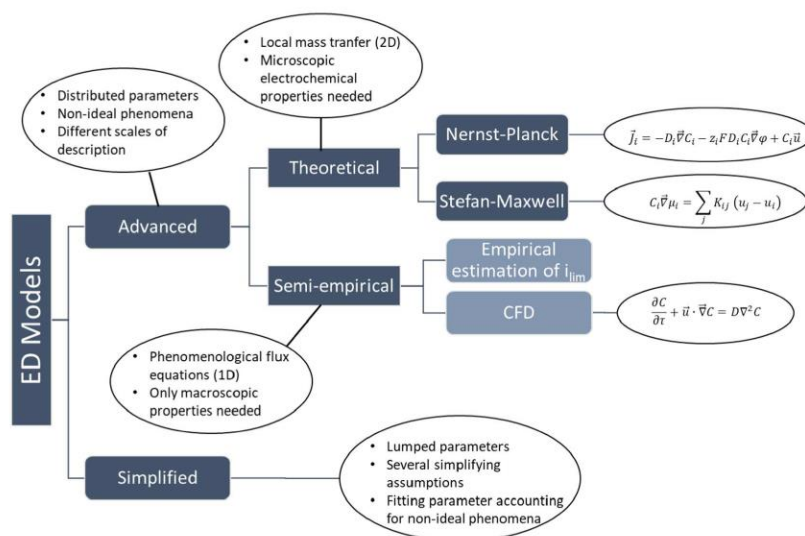


Figure 21. Block diagram showing the classification of modelling tools along with the main features of each class of models (Campione et al. 2018).

11.1. Nernst-Planck based Models

The most simplified models are 1-D (cross membrane) which simulate spacerless channels and predict the stack performance by lumped parameters. In other cases, variations along the stack length are taken into account in 2-D (axial + cross-membrane) by simulating the entire channel from inlet to outlet (stack performance predicted by distributed parameters along the axial direction). In some cases, fluid dynamics is explicitly simulated by the Navier-Stokes and continuity equations, while other models assume either a developed flow field with parabolic velocity profile (Hagen-Poiseuille equation), or even a flat profile. Differently, in Gurreri et al. (2017) a periodic portion of a single cell was simulated, thus allowing a very accurate spatial resolution, suitable for channels with either non-conducting spacers or membrane profiles, while keeping the total number of elements compatible with acceptable RAM requirements and computing time. Tado et al. (2016) simulated the spacer as a porous domain (Darcy's law) and integrated the governing equations over the channels width, thus obtaining a 1-D axial model. Enciso et al. (2017) performed 3-D simulations of a stack with spacerless channels by a simplified approach.

Some models have simulated the membranes as a domain with Ohmic behavior, i.e. by neglecting the effect of the concentration variations (secondary current distribution) and in some models membranes were not even included in the computational domain, but were modelled by imposing appropriate boundary conditions. Conversely, various simulation tools have explicitly simulated the membranes by the Nernst-Planck equation, taking into account the concentration variation. Water transport has been simulated only in a few cases. Clearly, the complete simulation including the membranes in the computational domain implies that all the coefficients characterizing the transport

through the membranes are known. Finally, several models were implemented in multi-physics modelling platforms based on the Finite Element Method (FEM).

Based on literature review, all models that simulate mass transport by the Nernst-Planck equation have been mostly focused on the membrane modeling, while only little attention has been paid to the modeling of overall process behavior for simulation and design purpose. As a consequence, hydrodynamics and associated phenomena of concentration polarization have been taken into account only by a simplified approach. These models have been implemented by either solver of differential equations or FEM-based software, which are devised for the simulation of simple geometries and would suffer from a prohibitively large memory requirement for the simulation of complex, accurately discretized, 3-D geometries even in the case of small periodic portion of a cell pair. For example, Gu et al. (2017) performed FEM simulations of a 3-D periodic domain of a spare-filled channel discretized with 1.4-2.9 million elements, simulating only convection-diffusion phenomena inside the channels. In this case, simulations took 3-8 h by using a workstation with 96 GB RAM. Therefore, building up a comprehensive simulation tool for an electromembrane process would be a very hard task and the direct simulation of the complete system by one single tool adopting the N-P approach appears to be almost impossible with currently available computing facilities.

11.2. Semi-empirical Models

As an alternative to the rigorous N-P models, several “semi-empirical” models have been developed, based on a mix of mass and energy balance equations, linking electrical and physical variables, and some empirical equations, which are able to predict the voltage drop over the cell pair and, in a more or less rigorous way, a number of physical phenomena characterizing the system. These models, that renounce to resolve the Nernst-Planck equation, simulate ion-exchange membranes by using only macroscopic, experimentally accessible, properties (such as transport numbers, Ohmic resistance, salt permeability, osmotic permeability), and allow the channel geometry to be taken into account in a more realistic way. In most cases, semi-empirical models are based on a system of algebraic and differential equations divided into:

- 1) Thermodynamic and electrical equations, leading to the calculation of cell pair potential and resistance, electric current, etc.;
- 2) Mass balance equations accounting for the variation of flow rates and concentrations along the main flow directions and strictly linked with mass transfer equations;
- 3) Transport equations providing mass flux of ions and water through the membrane, on the basis of empirical or separately calculated values for quantities like the Sherwood numbers;
- 4) Other equations allowing the calculation of macroscopic performance parameters such as power requirements, pumping losses, efficiencies, etc., on the basis of empirical or separately calculated values for quantities like the friction factors.

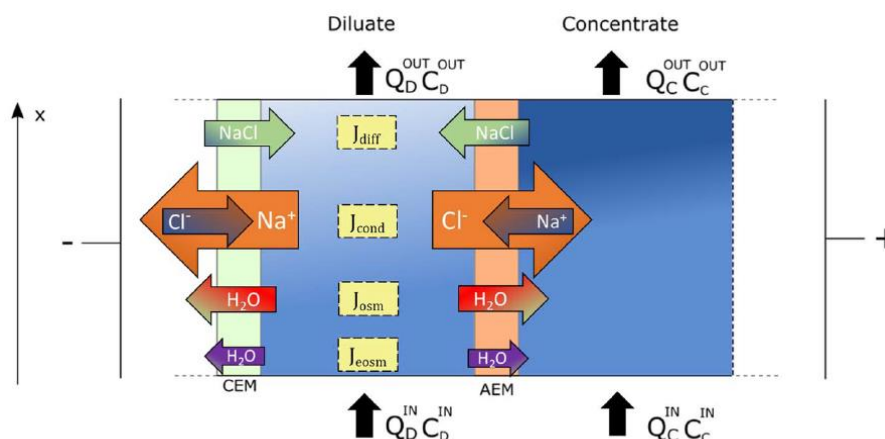


Figure 22. Schematic representation of the transport phenomena involved along the channels and through the membranes of an ED cell pair (Campione et al. 2018).

Most semi-empirical models are based on the segmentation modeling approach, which, in turn, can be supported either by experiments or by simulations providing Sherwood numbers. Phenomenological expressions of the mass fluxes can thus be written and can be linked to the mass balance equations for the simulation of the whole cell pair length. In particular, when fluid dynamics and mass transfer are simulated at small scale (channel repetitive unit, or unit cell) and the results are transferred to the higher scale at which mass balances and fluxes across the membranes apply (channel-scale, or meso-scale), a multi-scale model is obtained. This represents an integrated simulation tool, built on a hierarchical structure of scales, which can effectively address the full simulation problem.

11.3. Simplified Models for the Simulation and Design of ED Systems

The last class of models reported in the literature is characterized by a simplified structure. This approach has been mainly followed in order to implement models aiming at the preliminary design of ED units.

Lee et al. (2002) presented a design tool based on a number of simplifying assumptions and simple equations allowing to estimate the main features of an ED stack such as electric current and required membrane area for a fixed applied voltage. Aside from the model's simplicity, it considers various operating, performance and geometrical parameters such as ED stack construction, feed and product concentration, membrane properties, required membrane area and length, flow velocities, current density, recovery rate, energy consumption, etc. In particular, the main assumptions are:

1. Both cells have identical geometries and flow conditions;
2. The stack operates in a co-current flow;
3. The unit works below the limiting current density;
4. The membranes potential (back electro-motive force) is neglected;

5. Concentration polarization is neglected;
6. Diffusion of ions and water transport are neglected;
7. The current utilization factor is fixed.

However, the accuracy of this model is not high, especially for high salinity water. For this reason, Tsiakis and Papageorgiou (2005) and Qureshi and Zubair (2018) tried to improve the model accuracy while keeping it as simple as possible. In this regard, a substantial improvement in the Lee et al. (2002) model is still recommended (Qasem et al. 2018).

The more recent model presented by Veerman et al. (2011) was developed for river water and seawater as feed solutions, failed to predict the behaviour of the system in a wider range of operating conditions due to some simplifying assumptions and constitutive equations valid only in a limited concentration range. In fact, using higher salt concentration within the system can affect both membranes and solutions behaviour, increasing the complexity of the physical/mathematical description of the process. A recent model, based also on Veerman's approach, was developed by Tedesco et al. (2012), in which the authors attempted to extend the previous model to a wider range of concentration, giving a more general validity to the simulation tool developed. However, a number of non-ideal effects were still neglected in this latter model, such as the water transport through membranes (both osmotic and electro-osmotic fluxes), concentration polarisation phenomena and the presence of parasitic currents through manifolds (Tedesco et al. 2014).

Another example of simplified model was presented by Sadrzadeh et al. (2007). In this empirical regression-based model, a current efficiency is used to include all phenomena leading to an incomplete current utilization, without explicitly considering the various contributions different from the migrative flux for the mass transfer through membranes. In addition, membrane resistances as well as Nernst potentials are not explicitly calculated but all included in fitting parameters. The result is a lumped model characterized by a single equation that gives the outlet diluate concentration as a function of the various parameters.

Simplified models result in a limited number of equations that can easily be used to estimate the main design parameters. However, a simplified design tool does not provide details on the variables distribution along the channel, such as current profiles, and approximates all non-ideal phenomena governing the operation of real ED units. This represents the limitation when a model is needed to analyse the behavior of the ED process in detail, especially for optimization purpose. Another important limitation is represented by the fact that these model formulations strongly rely on experimentally fitted constants, implying that model has to be finely calibrated according to the specific unit to be simulated.

11.4. Proposed Electro-Dialysis numerical Model ($V_{\text{tank}}=cte$)

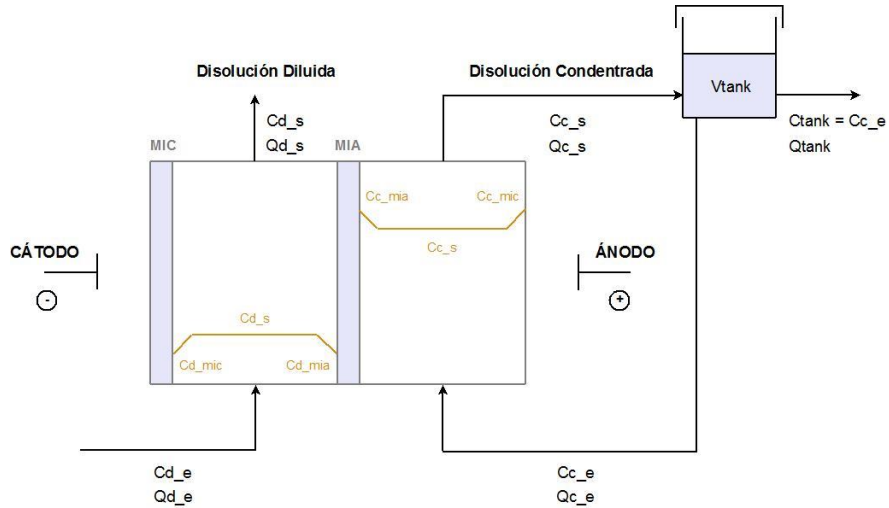
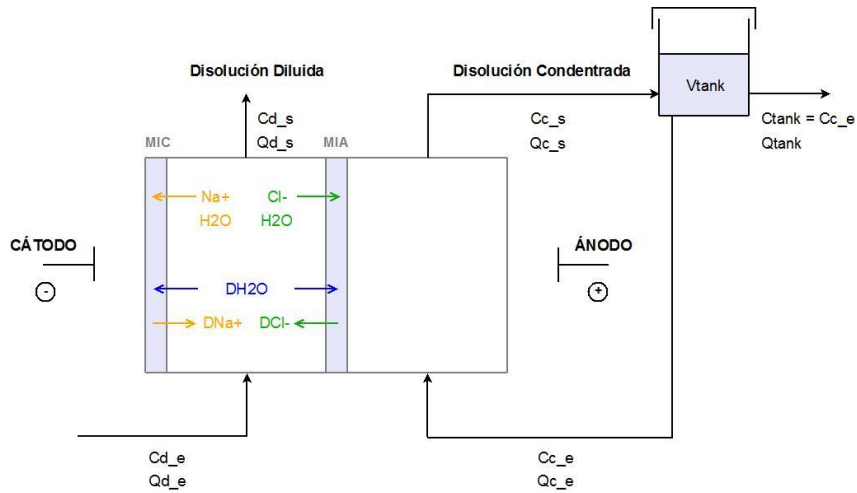


Figure 23: Flow diagram



- Ion migration

$$(11.1) \quad M = \frac{\eta \cdot I}{z \cdot F} \cdot 3600 \cdot N$$

- Electro-osmosis

$$(11.2) \quad M_w = t_w \cdot \frac{\eta \cdot I}{z \cdot F} \cdot 3600 \cdot N$$

- Ionic diffusion

$$(11.3)$$

$$D(t) = D_{Cl^-}(t) + D_{Na^+}(t) = \frac{D_{Cl^-_{mia}} \cdot S}{\sigma_{mia}} \cdot (C_{c_{mia}}(t) - C_{d_{mia}}(t)) \cdot 3600 \cdot N + \frac{D_{Na^+_{mic}} \cdot S}{\sigma_{mic}} \cdot (C_{c_{mic}}(t) - C_{d_{mic}}(t)) \cdot 3600 \cdot N$$

- **Osmosis**

$$(11.4) \quad D_w(t) = \frac{D_{w_mia} \cdot S}{\sigma_{mia}} \cdot (C_{c_mia}(t) - C_{d_mia}(t)) \cdot 3600 \cdot N + \frac{D_{w_mic} \cdot S}{\sigma_{mic}} \cdot (C_{c_mic}(t) - C_{d_mic}(t)) \cdot 3600 \cdot N$$

- **Mass balance on the shared N compartments of concentrated solution**

$$(11.5) \quad Q_{c_e} + Q_w(t) = Q_{c_s}(t)$$

$$(11.6) \quad Q_w(t) = (M_w + D_w(t)) \cdot \frac{M_{m-w}}{\rho_w}$$

$$(11.7) \quad C_{c_e}(t) \cdot Q_{c_e} + M = C_{c_s}(t) \cdot Q_{c_s}(t) + N \cdot V_{celda} \cdot \frac{dC_{c_s}(t)}{dt} + D(t)$$

- **Mass balance on the N compartments of diluted solution**

$$(11.8) \quad Q_{d_e} = Q_{d_s}(t) + Q_w(t)$$

$$(11.9) \quad C_{d_e}(t) \cdot Q_{d_e} + D(t) = C_{d_s}(t) \cdot Q_{d_s}(t) + N \cdot V_{celda} \cdot \frac{dC_{d_s}(t)}{dt} + M$$

- **Mass balance at the concentrated solution tank**

$$(11.10) \quad Q_{tank}(t) = Q_w(t)$$

$$(11.11) \quad C_{c_s}(t) \cdot Q_{c_s}(t) = C_{c_e}(t) \cdot Q_{c_e} + C_{c_e}(t) \cdot Q_{tank}(t) + V_{tank} \cdot \frac{d(C_{c_e}(t))}{dt}$$

- **Membrane Surface Concentration**

$$(11.12) \quad C_{d_mia}(t) = C_{d_s}(t) - \frac{(1 - t_{Cl}) \cdot \eta \cdot l}{z \cdot F \cdot k_m \cdot S}$$

$$(11.13) \quad C_{c_mia}(t) = C_{c_s}(t) + \frac{(1 - t_{Cl}) \cdot \eta \cdot l}{z \cdot F \cdot k_m \cdot S}$$

$$(11.14) \quad C_{d_mic}(t) = C_{d_s}(t) - \frac{(1 - t_{Na}) \cdot \eta \cdot I}{z \cdot F \cdot k_m \cdot S}$$

$$(11.15) \quad C_{c_mic}(t) = C_{c_s}(t) + \frac{(1 - t_{Na}) \cdot \eta \cdot I}{z \cdot F \cdot k_m \cdot S}$$

- **Unknown Variables**

$M \equiv$ Ionic migration, $\frac{mol NaCl}{h}$

$M_w \equiv$ Electro-osmosis migration, $\frac{mol H_2O}{h}$

$D \equiv$ Ionic diffusion, $\frac{mol NaCl}{h}$

$D_w \equiv$ Water diffusion (osmosis), $\frac{mol H_2O}{h}$

$C_{d_s} \equiv$ Outlet concentration of the diluted compartments, $\frac{mol NaCl}{L}$

$Q_{d_s} \equiv$ Outflow of the diluted compartments, $\frac{L}{h}$

$C_{c_e} \equiv$ Inlet concentration of the concentrate compartments, $\frac{mol NaCl}{L}$

$C_{c_s} \equiv$ Outlet Concentration of the compartments of concentrate, $\frac{mol NaCl}{L}$

$Q_{c_s} \equiv$ Output flow of the concentrate compartments, $\frac{L}{h}$

$Q_w \equiv$ Water flow that is transmitted from the diluted compartments to those of adjacent concentrates, $\frac{L}{h}$

$Q_{tank} \equiv$ Water flow that overflows from tank, $\frac{L}{h}$

$C_{d_mia} \equiv$ Concentration on the surface of the anion exchange membranes (MIA) on the side of the diluted compartments, $\frac{mol NaCl}{L}$

C_{c_mia} \equiv Concentration on the surface of the MIAs on the side of the concentrate compartments,
 $\text{mol NaCl} / \text{L}$

C_{d_mic} \equiv Concentration on the surface of the cation exchange membranes (MIC) on the side of the
 diluted compartments, $\text{mol NaCl} / \text{L}$

C_{c_mic} \equiv Concentration on the surface of the MICs on the side of the concentrate compartments,
 $\text{mol NaCl} / \text{L}$

(15 equations = 15 unknown variables)

- **Inputs: user defined variables**

I \equiv Current Intensity, A

C_{d_e} \equiv Inlet concentration of the diluted compartments, $\text{mol NaCl} / \text{L}$

Q_{d_e} \equiv Inlet flow of the concentrate compartments, L / h

Q_{c_e} \equiv Inlet flow of the concentrate compartments, L / h

- **Parameters**

M_{m_w} \equiv Molecular mass of water, $\text{g H}_2\text{O} / \text{mol H}_2\text{O}$

ρ_w \equiv Water density, $\text{g H}_2\text{O} / \text{L H}_2\text{O}$

F \equiv Faraday constant, C / mole^-

z \equiv Ionic charge NaCl, adim

N \equiv Number of stack cells, adim

σ_{mia} \equiv MIA thickness, dm

σ_{mic} \equiv MIC thickness, dm

k_m \equiv Mass transfer coefficient, dm / s

$L \equiv$ Length of the compartments or spacing between membranes, dm

$S \equiv$ Effective section of the membranes, dm^2

$V_{celda} \equiv$ Cell volume, L

$$V_{celda} = L \cdot S$$

$V_{tank} \equiv$ Volume of concentrate tank, L

$D_{Cl_mia} \equiv$ Coefficient of diffusion of anions (Cl⁻) through the MIA, dm^2/s

$D_{Na_mic} \equiv$ Coefficient of diffusion of the cations (Na⁺) through the MIC, dm^2/s

$D_{w_mia} \equiv$ Coefficient of diffusion of water through the MIA, dm^2/s

$D_{w_mic} \equiv$ Coefficient of water diffusion through MIC, dm^2/s

$t_{Cl} \equiv$ Anion transport number (Cl⁻), $adim$

$t_{Na} \equiv$ Cationic transport number (Na⁺), $adim$

$t_w \equiv$ Water transport number, $adim$

$$t_w = h_{Na} + h_{Cl}$$

$h_{Na} \equiv$ Primary hydration number for the Na⁺ ion, $adim$

$h_{Cl} \equiv$ Primary hydration number for the Cl⁻ ion, $adim$

$\eta \equiv$ Electrical efficiency, $adim$

$$\eta = t_{Cl_mia} + t_{Na_mic}$$

$t_{Cl_mia} \equiv$ Anionic transport number in MIAs, $adim$

$t_{Na_mic} \equiv$ Number of cationic transport in the MIC, $adim$

11.5. Renewable Energy Integration

Continued dependence of separation processes to produce salt on non-renewable energy sources is no longer a sustainable practice due to the risk of depletion of available energy sources and increase

of greenhouse gas emissions. It is crucial to develop processes that are renewable and sustainable for water treatment processes. The following options are available for managing the water and energy crisis in a sustainable manner:

1. Utilize renewable energy sources,
2. Implement process hybridization,
3. Develop low-cost and energy-efficient technologies,
4. Reuse water.

The primary energy requirement of ED process is the direct current (DC) used to separate the salt ions. Power consumption is required for the low pressure pump used to circulate water through the narrow chambers. When high total dissolved solids feed water is used, the DC consumption will rapidly increase, which results in a high cost of desalinated water. ED can produce water with a high recovery ratio of about 85-94% for one stage, can be operated at low pressure, needs low chemical usage, and can be used to treat water with high levels of suspended solids. The major problem to be expected in electrodialysis systems is the possible occurrence of leaks in the membrane stacks. The total power consumption of ED units ranges from 0.7 to 2.5 kWh/m³ of desalinated water for feed water salinity of 2500 ppm and from 2.64–5.5 kWh/m³ of desalinated water for feed water salinity of 5000 ppm (Al-Qaraghuli and Kazmerski 2012).

Most of the studies carried out on ED over the last 40 years focused on the conventional mode of operation where a constant voltage or current source is used for operating the membrane system. The available studies on renewable energy powered ED technologies are very limited. Furthermore, the opportunity to produce electricity by means of energy conversion processes (ORC) using available waste heat recovery systems will be object of study in future deliverables. This complementary analysis, altogether with a numerical modeling of the ED will allow to analyse the energy savings potential for a specific site and operating conditions.

11.6. Deliverables

Deliverables will compile the technical data produced once this data has been processed. Deliverables can be shared with other partners based in their confidentiality. All the deliverables will be uploaded to the European Union Website.

12. RCE Integration

12.1. RCE

In ZEROBrine, several different groups of scientists provide specialized tools for specific tasks. These tools have to be integrated into one single software to be used together in the envisioned scientific projects. Furthermore the tools need to be accessible to everyone inside of the project without

additional overhead or maintenance effort. To address this requirement the RCE Framework was adapted to suit the needs of the ZEROBrine Project and to make the developed tools easily available.

RCE was developed at DLR as an open source, freely available, platform independent and distributed integration environment for scientists and engineers to analyze, optimize, and design complex systems. RCE provides a platform for sharing different tools from different teams within the project, grouping them into functional workflows that can be executed automatically. As each tool has to be integrated only once to be accessible to everyone in the project, both the maintenance and the integration effort are low and manageable. Therefore RCE is fulfilling the requirements detailed above.

RCE provides a reliable method to couple tools of different kinds into one functional super-model or simulation. Each tool is represented as a block that can be connected to other blocks. Each block represents a tool, each connection an exchange of data. This creates a workflow which can be executed at the push of one button. Due to its distributed nature, tools can be used both locally and remotely by the internet at the same time in the same workflow.

RCE is extensible and supports different scientific applications with a wide range of requirements. Coupling of external tools into workflows is a central feature of RCE and as each tool or model has to be integrated only once to be accessed using standardized inputs and outputs throughout a network of RCE servers by RCE clients, it adds as low overhead to the development of tools. Each tool output can be configured to be passed along the workflow as input to another tool or as results for storage to disk.

A tool is executed by RCE once all required input data is available, either from other tools or provided by the user. Tool and workflow execution is therefore automated, so no user interaction is required during execution. Result data are generated by the tools of a workflow during its execution and collected by RCE, which provides them in a graphical viewer to the scientist or as data files.

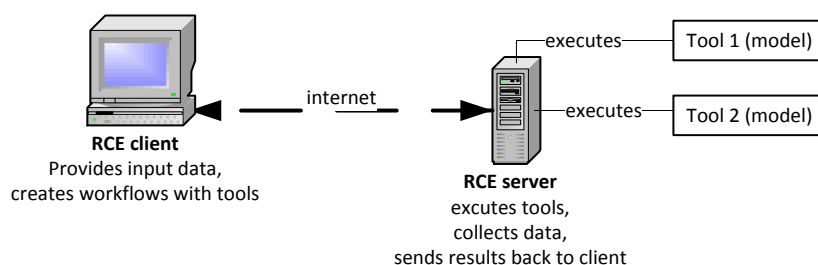
In complex analysis, design, or simulation tasks like it is the case in ZEROBrine, multiple experts and tools are involved, which are located at different sites. To support collaboration, RCE is designed in two components, a server and a client. The servers host integrated tools and make them available to clients of scientists and engineers in a peer-to-peer network.

12.2. RCE Server

The RCE server is the heart of the integration environment, as it provides access to all tools integrated into it. The RCE server is only responsible for executing (partial) workflows, collecting results and handing them off to the client and therefore does not feature the graphical user interface provided by the RCE client. The RCE server is run on dedicated hardware, as it does all calculations of the tools it provides access to. Within the RCE server, tools can be integrated, as long as they do not require user input through a graphical user interface at runtime. All tools with command line interfaces, no matter the programming language, can be integrated via a flexible scripting interface based on Python within RCE.

The tools can then be accessed by RCE clients remotely and via their respective graphical user interfaces. The tools on the RCE server can be chained into workflows by the users through the client and executed as if they were one large program. The RCE server provides its integrated tools as building blocks. It manages data transfer between the users and in between tools. As a data driven environment, the server automatically executes tools, when the prerequisite data is available and collects the output. Output can be represented to the user via the graphical user interface of the client or as data files.

If multiple RCE servers are available, they can be connected into one network, providing their respective tools like one seamless single program to all connected clients. All data handling during execution of workflows is done by RCE without the need of interference by the user. RCE servers are responsible only for executing their tools and for transferring the created data. Workflows can be defined including tools hosted on multiple servers, in the same way, as if all tools were available on one single server or locally on the client.



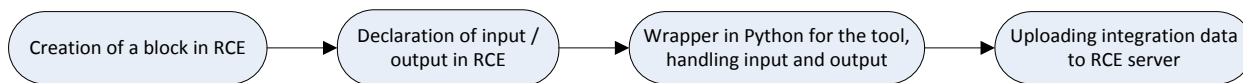
12.3. The RCE Client

The RCE client software features a graphical user interface for designing workflows and for tool integration. Users can either use it locally, with local tools integrated to RCE executing local workflows. Or they can connect to one or a network of remote RCE server by the internet. Then the client has access to all tools locally in the client and remotely on each RCE server. The user can then create workflows from all available tools. All data transfer is handled by RCE and protected by encryption and automated without the need of user interaction. The scientist can therefore focus solely on creating workflows out of the available tools and executing them.

12.4. Tool Integration

Tools are easily integrated into RCE with a graphical tool provided by the client. The integrated tool can then be transferred to an RCE server to be made available to all clients, or used locally only in this RCE client. Within RCE the first step to integrate a tool, is the creation of a new block. The block later represents the tool in workflows and can be used in the graphical user interface. The block can be configured with all inputs and outputs needed by the tool. This allows RCE to check for inputs and outputs automatically during execution and enables RCE to start the tool when all required data is available. Integration is a simple task of writing minimal Python wrappers feeding the inputs from RCE toward the tool and the output of the tool backward to RCE. Data can be cleaned, reshaped and

adapted to the tool from within Python at this step if necessary. Afterwards the tool represented by its block is available for execution in workflows.



12.5. Technical Aspects of RCE

RCE is written in Java and therefore platform independent. It can be installed and executed both on linux, mac and windows operating systems and is capable of serving tools between these platforms. Thus RCE is capable of integrating platform depending tools into one seamless tool that can be easily accessed by scientists through their RCE clients.

RCE is shipped only as one single java software package. It can be configured to either run as a server or as a client. This supports tool integration as the tool can first be integrated in client mode and then RCE can be started in server mode with the integrated tool, rendering a transfer of the integration data to the server superfluous.

12.6. Progress on the RCE Integration of Tools

As part of the work package we set up an RCE server at University Stuttgart. Due to IT security regulations and firewall limitations, all clients will need fixed ip addresses to be allowed to connect to the RCE server, which have to be declared in advanced to DLR. On the RCE server we currently integrated one testing model as a tool ready to use in workflows. We successfully wrote a wrapper around the model to feed in the input data and feedback the output data to RCE. The model was tested locally and on the server. It is now available on the RCE server and may be accessed via registered clients through the internet for integration into workflows. The tool will serve as a basis the common simulation activities within the framework of WP7.

Further tools from other researchers in ZEROBrine can either be integrated into the Stuttgart RCE server or the RCE software can be provided to them for setup of their own dedicated RCE server at their respective sites.

13. Bibliography

- Alamdari, A., M. R. Rahimpour, N. Esfandiari, and E. Nourafkan. 2008. Kinetics of magnesium hydroxide precipitation from sea bittern. *Chemical Engineering and Processing* 47:215–221.
- Alexandratos, S. D. 2009. Ion-Exchange Resins: A Retrospective from Industrial and Engineering Chemistry Research. *Ind. Eng. Chem. Res.* 48:388–398.
- Ali, N., A. W. Mohammad, and A. L. Ahmad. 2005. Use of nanofiltration predictive model for membrane selection and system cost assessment. *Separation and Purification Technology* 41:29–37.

- Alkaisi, A., R. Mossad, and A. Sharifian-Barforoush. 2017. A review of the water desalination systems integrated with renewable energy. *Energy Procedia* 110, 268–274.
- Alkhudhiri, A., N. Darwish, and N. Hilal. 2012. Membrane distillation: A comprehensive review. *Desalination* 287:2–18.
- AlMadani, H. M. N.. 2003. Water desalination by solar powered electro dialysis process. *Renewable Energy*, 28:1915–1924.
- Andrjesdottir, O., C. L. Ong, M. Nabavi, S. Paredes, A. S. G. Khalil, B. Michel, and D. Poulikakos. 2013. An experimentally optimized model for heat and mass transfer in direct contact membrane distillation. *International Journal of Heat and Mass Transfer* 66:855–867.
- Bowen, W. R., B. Cassey, P. Jones, and D. L. Oatley. 2004. Modelling the performance of membrane nanofiltration—application to an industrially relevant separation. *Journal of Membrane Science* 242:211–220.
- Bowen, W. R., A. W. Mohammad, and N. Hilal. 1997. Characterisation of nanofiltration membranes for predictive purposes — use of salts, uncharged solutes and atomic force microscopy. *Journal of Membrane Science* 126:91–105.
- Campione, A., L. Gurreri, M. Ciofalo, G. Micale, A. Tamburini, and A. Cipollina. 2018. Electrodialysis for water desalination: A critical assessment of recent developments on process fundamentals, models and applications. *Desalination*, 434: 121–160.
- Carta, J., J. González, and V. Subiela. 2004. The SDAWES project: an ambitious R&D prototype for wind-powered desalination. *Desalination*, 161(1): 33–48.
- Cipollina, A., M. Bevacqua, P. Dolcimascolo, A. Tamburini, A. Brucato, H. Glade, L. Buether, and G. Micale. 2014. Reactive crystallisation process for magnesium recovery from concentrated brines. *Desalination and Water Treatment*:1–12.
- DOWEX Ion Exchange Resins Water Conditioning Manual. (n.d.). .
- DOWEX Marathon C Resin - Product Data Sheet. (n.d.). .
- El-Dessouki, H. T., and H. M. Ettouney. 2002. *Fundamentals of Salt Water Desalination*. . Elsevier.
- El-Dessouky, H., I. Alatiqi, S. Bingulac, and H. Ettouney. 1998. Steady-State Analysis of the Multiple Effect Evaporation Desalination Process. *Chem. Eng. Technol.* 21:437–451.
- Enciso, R., J.A. Delgadillo, O. Domínguez, and I. Rodríguez-Torres. 2017. Analysis and validation of the hydrodynamics of an electro dialysis cell using computational fluid dynamics. *Desalination*, 408: 127–132.
- ESDU. 1993. *Condensation inside tubes: pressure drop in straight horizontal tubes*. ESDU Series on Heat Transfer.
- Eykens, L., I. Hitsov, K. De Sitter, C. Dotremont, L. Pinoy, I. Nopens, and B. Van der Bruggen. 2016. Influence of membrane thickness and process conditions on direct contact membrane distillation at different salinities. *Journal of Membrane Science* 498:353–364.
- Fernandez-Gonzalez, C., A. Dominguez-Ramos, R. Ibañez, and Irabien, A.. 2015. Sustainability assessment of electro dialysis powered by photovoltaic solar energy for freshwater production. *Renewable and Sustainable Energy Reviews* 47, 604–615.
- Filmtec Reverse Osmosis Membranes Technical Manual. (n.d.).
- Geraldes, V., and M. D. Afonso. 2006. Generalized Mass-Transfer Correction Factor for Nanofiltration and Reverse Osmosis. *AIChE Journal* 52:3353–3362.
- Geraldes, V., and A. M. B. Alves. 2008. Computer program for simulation of mass transport in nanofiltration membranes. *Journal of Membrane Science* 321:172–182.
- Gu, B., C.S. Adjiman, X.Y. Xu. 2017. The effect of feed spacer geometry on membrane performance and concentration polarisation based on 3D CFD simulations. *J. Membr. Sci.*, 527: 78–91.
- Gude, V.G., N. Nirmalakhandan, S. Deng. 2010. Renewable and sustainable approaches for desalination. *Renewable and Sustainable Energy Reviews* 14, 2641–2654.
- Gurreri, L., G. Battaglia, A. Tamburini, A. Cipollina, G. Micale, M. Ciofalo. 2017. Multiphysical modelling of reverse electro dialysis. *Desalination*, 423: 52–64..

- Hasan, M. and M. Louhi-Kultanen, Ice growth kinetics modeling of air-cooled layer crystallization from sodium sulfate solutions, *Chem. Eng. Sci.* 133 (2015) 44-53.
- Hasan, M., R. Filimonov, J. Chivavava, J. Sorvari, M. Louhi-Kultanen, and A. Emslie Lewis. Ice growth on the cooling surface in a jacketed and stirred eutectic freeze crystallizer of aqueous Na₂SO₄ solutions. *Separation and Purification Technology* 175 (2017) 512–526.
- Hassan, A. S., and M. A. Darwish. 2014. Performarce of thermal vapor compression. *Desalination* 335:41–46.
- Hitsov, I., L. Eykens, W. De Schepper, K. De Sitter, C. Dotremont, and I. Nopens. 2017. Full-scale direct contact membrane distillation (DCMD) model including membrane compaction effect. *Journal of Membrane Science* 524:245–256.
- Hitsov, I., T. Maere, K. De Sitter, C. Dotremont, and I. Nopens. 2015. Modelling approaches in membrane distillation: A critical review. *Separation and Purification Technology* 142:48–64.
- Hitsov, I., K. De Sitter, C. Dotremont, and I. Nopens. 2018. Economic modelling and model-based process optimization of membrane distillation. *Desalination* 436:125–143.
- Ishimaru, N.. 1994. Solar photovoltaic desalination of brackish-water in remote areas by electrodiagnosis. *Desalination*, 98 (1–3): 485–493.
- Jamal, K., M. A. Khan, and M. Kamil. 2004. Mathematical modeling of reverse osmosis systems. *Desalination* 160:29–42.
- Khalifa, A., H. Ahmad, M. Antar, T. Laoui, and M. Khayet. 2017. Experimental and theoretical investigations on water desalination using direct contact membrane distillation. *Desalination* 404:22–34.
- Khayet, M., A. Velasquez, and J. I. Mengual. 2004. Modelling mass transport through a porous partition: Effect of pore size distribution. *Journal of Non-Equilibrium Thermodynamics* 29:279–299.
- Kimura, S., and S. Sourirajan. 1967. Analysis of data in reverse osmosis with porous cellulose acetate membrane used. *AIChE Journal* 13:497–503.
- Kucera J. 2014. *Desalination: Water from water*. Scrivener Publishing.
- Lee, H., F. Sarfert, H. Strathmann, S.H. Moon. 2002. Designing of an electrodiagnosis desalination plant. *Desalination*, 142: 267–286.
- Liu, Z., L. Li, Y. Chen, X. Li, Y. Zhang, and G. Shen. 2011. Optimal parameters of response surface methodology for precipitation of magnesium hydroxide flame retardant. *Chin. J. Process Eng.* 11:1017–1023.
- Lundstrom, J.E.. 1979. Water desalting by solar powered electrodiagnosis. *Desalination*, 31 (1–3): 469–488.
- Lonsdale, H. K., U. Merten, and R. L. Riley. 1965. Transport properties of cellulose acetate osmotic membranes. *Journal of Applied Polymer Science* 9:1341–1362.
- M. Bialik, P. Sedin, and H. Theliander. 2008. Boiling Point Rise Calculations in Sodium Salt Solutions. *Ind. Eng. Chem. Res.* 47:1283–1287.
- Malek, A., M. N. . Hawlader, and J. C. Ho. 1996. Design and Economics of RO seawater desalination. *Desalination* 105:245–261.
- Malek, P., J.M. Ortiz, and H.M.A. Schulte-Herbrüggen. 2016. Decentralized desalination of brackish water using an electrodiagnosis system directly powered by wind energy. *Desalination*, 377, 54–64.
- Marchisio, D. L., J. T. Pikturna, m R. O. Fox, R. D. Vigil, and A. A. Barresi. 2003a. Quadrature Method of Moments for Population-Balance Equations. *AIChE Journal* 49:1266–1276.
- Marchisio, D. L., R. D. Vigil, and R. O. Fox. 2003b. Quadrature method of moments for aggregation-breakage processes. *Journal of Colloid and Interface Science* 258:322–334.
- Moser, M. 2015. *Combined Electricity and Water Production Based on Solar Energy*. Institut für Energiespeicherung der Universität Stuttgart.

- Oatley, D. L., L. Llenas, R. Pérez, P. M. Williams, X. Martínez-Lladó, and M. Rovira. 2012. Review of the dielectric properties of nanofiltration membranes and verification of the single oriented layer approximation. *Advances in Colloid and Interface Science* 173:1–11.
- Al-Obaidani, S., E. Curcio, F. Macedonio, G. Di Profio, H. Al-Hinai, and E. Drioli. 2008. Potential of membrane distillation in seawater desalination: Thermal efficiency, sensitivity study and cost estimation. *Journal of Membrane Science* 323:85–98.
- Omar, H. M., and S. Rohani. 2017. Crystal Population Balance Formulation and Solution Methods: A review. *Crystal Growth and Design* 17:4028–4041.
- Ortega-Delgado, B., L. Garcia-Rodriguez, and D. C. Alarcon-Padilla. 2017. Opportunities of improvement of the MED seawater desalination process by pretreatments allowing high-temperature operation. *Desalination and Water Treatment*, 97:94–108.
- Ortiz, J. M., E. Expósito, F. Gallud, V. García García, V. Montiel, A. Aldaz. 2006. Photovoltaic electro dialysis system for brackish water desalination: Modeling of global process, *J. Membr. Sci.*, 274: 138–149.
- Pitzer, K. S., and G. Mayorga. 1973. Thermodynamics of Electrolytes. I I. Activity and Osmotic Coefficients for Strong Electrolytes with One or Both Ions Univalent. *The Journal of Physical Chemistry* 77:2300–2308.
- Al-Qaraghuli, A. and L.L. Kazmerski. 2012. Comparison of technical and economic performance of the main desalination processes with and without renewable energy coupling. *Proceedings of the American Solar Energy Society World Renewable Energy Forum*, 1–8.
- Qasem, N.A.A., B. Ahmed Qureshi, and S.M. Zubair. 2018. Improvement in design of electro dialysis plants by considering the Donnan potential. *Desalination*, 441: 62–76.
- Qtaishat, M., T. Matsuura, B. Kruczek, and M. Khayet. 2008. Heat and mass transfer analysis in direct contact membrane distillation. *Desalination* 219:272–292.
- Qureshi, B.A. and Zubair, S.M.. 2018. Design of electro dialysis desalination plants by considering dimensionless groups and variable equivalent conductivity. *Desalination*, 430: 197–207.
- Roy, Y., M. H. Sharqawy, and J. H. Lienhard. 2015. Modeling of flat-sheet and spiral-wound nanofiltration configurations and its application in seawater nanofiltration. *Journal of Membrane Science* 493:360–372.
- Sadrzadeh, M., A. Kaviani, and T. Mohammadi. 2007. Mathematical modeling of desalination by electro dialysis. *Desalination*, 206: 538–546.
- Senthilmurugan, S., A. Ahluwalia, and S. K. Gupta. 2005. Modeling of a spiral-wound module and estimation of model parameters using numerical techniques. *Desalination* 173:269–286.
- Sharqawy, M. H., J. H. Lienhard V, and S. M. Zubair. 2010. The thermophysical properties of seawater: A review of existing correlations and data. *Desalination and Water Treatment* 16:354–380.
- Shen, S. 2015. Thermodynamic Losses in Multi-effect Distillation Process. *Materials Science and Engineering* 88:1–12.
- Sommariva, C. 2010. *Desalination and Advanced Water Treatment-Economics and Financing*. . Balaban Desalination Publications.
- Tado, K., F. Sakai, Y. Sano, and A. Nakayama. 2016. An analysis on ion transport process in electro dialysis desalination, *Desalination* 378: 60–66.
- Tedesco, M., A. Cipollina, A. Tamburini, W. van Baak, and G. Micale. 2012. Modelling the reverse electro dialysis process with seawater and concentrated brines. *Desalination Water Treat.* 49: 404–424.
- Tedesco, M., A. Cipollina, A. Tamburini, I.D.L. Bogle, and G. Micale. 2015. A simulation tool for analysis and design of reverse electro dialysis using concentrated brines. *Chemical Engineering Research and Design* 93: 441–456.
- Tsiakis, P. and L.G. Papageorgiou. 2005. Optimal design of an electro dialysis brackish water desalination plant. *Desalination*, 173: 173–186.
- Turek, M., and W. Gnot. 1995. Precipitation of magnesium hydroxide from brine. *Ind. Eng. Chem. Res* 34:244–250.

- Veerman, J., M. Saakes, S.J. Metz, and G.J. Harmsen. 2011. Reverse electrodialysis: a validated process model for design and optimization. *Chem. Eng. J.* 166: 256–268.
- Veza, J., B. Peñate, and F. Castellano. 2004. Electrodialysis desalination designed for off-grid wind energy. *Desalination*, 160 (3): 211–221.
- Vezzani, D., and S. Bandini. 2002. Donnan equilibrium and dielectric exclusion for characterization of nanofiltration membranes. *Desalination* 149:477–483.
- Vince, F., F. Marechal, E. Aoustin, and P. Breant. 2008. Multi-objective optimization of RO desalination plants. *Desalination* 222:96–118.
- Wheaton, R., and L. Lefevre. 2016. *DOWEX Ion Exchange Resins - Fundamental of Ion Exchange*. . Dow Chemical Company.
- Wilf, M. 2007. *The Guidebook to Membrane Desalination Technology*. . Balaban Desalination Publications.
